Summer 2021

Modeling Interactions in Concentrated Ceramic Suspensions Under AC Electric Field

Naga Bharath Gundrati
Old Dominion University, bharath211293@gmail.com

MODELING INTERACTIONS IN CONCENTRATED CERAMIC SUSPENSIONS UNDER AC ELECTRIC FIELD

by

Naga Bharath Gundrati
B.Tech. May 2015, SRM University, India
M.S. May 2017, State University of New York

A Thesis Submitted to the Faculty of
Old Dominion University in Partial Fulfilment of
Requirements for the Degree of

MASTER OF SCIENCE

MECHANICAL & AEROSPACE ENGINEERING

OLD DOMINION UNIVERSITY
August 2021

Approved by:

Dipankar Ghosh (Co-Director)

Shizhi Qian (Co-Director)

Xiaoyu Zhang (Member)

Yan Peng (Member)

ABSTRACT

MODELING INTERACTIONS IN CONCENTRATED CERAMIC SUSPENSIONS UNDER AC ELECTRIC FIELD

Naga Bharath Gundrati
Old Dominion University, 2021
Co-Directors: Dr. Dipankar Ghosh
Dr. Shizhi Qian

Colloidal processing of ceramics manipulates the interaction forces using additives or external energy field between the suspending particles to fabricate complex structures. Under AC electric field, mutual dielectrophoretic (DEP) forces between particles create particle chaining. Dielectrophoresis (DEP) is adopted to control ceramic particles in the colloidal suspension, which can benefit from employing DEP forces to externally control the fabrication of ceramic materials with desired porosity and hierarchical structure. To this end, it is crucial to understand the interactions between ceramic particles in aqueous media and AC electric field. The dynamic interactions of ceramic particles under AC electric field are modelled using the iterative dipole moment (IDM) method, which was first validated by the Maxwell stress tensor (MST) method. The IDM method has the capability to simulate the field-particle interactions and formation of particle chains for large number of ceramic particles in aqueous media. The DEP assembly of ceramic particles is investigated as functions of the frequency of the applied electric field, initial particle distribution, electric properties of ceramic particles and composition of the ceramic suspension.

The quantitative analysis of particle cluster formation and the particle packing analysis of the particle distribution at the end of the simulation using electric field distribution and Voronoi

diagrams provide insights into the effect of AC DEP on large number of particles. The DEP induced particle interactive motion is observed to create interconnected particle clusters concentrated in the center of the domain or graded structure with alternating dense and sparse regions depending on the material type and composition of the ceramic suspension.

This thesis is dedicated to my teachers, friends, and family.

ACKNOWLEDGEMENTS

First and foremost, I would like to express my utmost gratitude to Dr. Dipankar Ghosh for his continuous support and motivation during the course of my research. I am grateful for the substantial amount of dedication and patience he extended through my difficult time while working on the thesis. I am deeply honored to be one of his students. I am indebted to the valuable time and gentle criticism offered by my co-advisor Dr. Shizhi Qian which helped me complete the thesis on time. I would also like to thank Dr. Sebastian Bawab and the Mechanical Engineering department for funding my education and giving me a chance to work as a graduate teaching assistant.

My utmost respect and gratitude must be paid to my friends and colleagues, Sashanka Akurati, Rohan Parai, Mahesh Banda and, Diego A. Terrones, for providing me with invaluable knowledge, giving me technical advice, and motivating me this whole time. I would like to acknowledge Dr. Xiaoyu Zhang and Dr. Yan Peng for agreeing to be on my thesis committee despite their exhausting schedules.

I am extremely thankful to all these people without whom my journey at Old Dominion University would not have been complete. Last but not least, I would like to express my profound love and gratitude for my friends and family.

NOMENCLATURE

V_A	Van der Walls energy
V_B	Electrostatic double layer force
V_T	Interaction energy
E_B	Energy barrier
L_x	Width of the domain
L_y	Length of the domain
a	Particle radius
d	Inter particle distance
w	Distance from the wall or electrode
$\tilde{E}$	Electric field
$\tilde{p}_i$	Dipole moment
$K_i(\omega)$	Claussius- Mossotti factor
$\tilde{\varepsilon}_p$	Complex permittivity of particle
$\tilde{\varepsilon}_m$	Complex permittivity of medium
ε_p	Permittivity of particle
ε_m	Permittivity of medium
σ_p	Conductivity of particle
σ_m	Conductivity of medium
f	Frequency of AC electric field
ω	Angular frequency
$\tilde{\varphi}$	Dipole induced electric field

NOMENCLATURE

r	Position vector between two particles
F_{dep}	Dielectrophoretic force
F_{drag}	Hydrodynamic drag force
F_{dep}	Dielectrophoretic force
$F_{rep,\ p-p}$	Repulsive force between particles
$F_{rep,\ p-w}$	Repulsive force between particle and wall/ electrode
F_p and F_w	Spring constant for repulsive force
F_{tot}	Total force acting on particle
δ_p	Minimum interparticle separation distance
κ_p and κ_w	Range constant for repulsive force
m_p	Mass of particle
ρ_p	Density of particle
t	Time step
v	Velocity of particle
CN	Coordination number
CN_{avg}	Average coordination number

TABLE OF CONTENTS

Page

Page

LIST OF TABLES

LIST OF FIGURES

Figure Page

Figure Page

I. INTRODUCTION

A wide range of unique fabrication processes of ceramic structures are subject to extensive research as they offer many distinct advantages over polymers or metals such as hardness, chemical inertness, and low fracture toughness, that are essential to many applications such as cutting tools, heat engine parts, body implants, sensors, capacitors and actuators, with new applications evolving continuously [1]. Mankind has used ceramics for thousands of years dating back to almost 6000 B.C in China. The traditional ceramics based on naturally occurring materials form the basis for cookware, household items, and works of art. Advanced ceramics are produced from chemically synthesized micro- or nano- scaled non-metallic/metal oxides [2]. These ceramics provide superior thermal stability, corrosion and wear resistance, and low density.

Ceramic materials have traditionally been synthesized by fusion or sintering of complex mixtures in powder form. The powder processing techniques of ceramics involve powder synthesis, preparation of powder for consolidation, followed by consolidation into desired shape and size. The formed 'green body' is sintered at high temperature to achieve final microstructure and properties. The defects that arise from the powder processing of ceramics especially in dry pressing become fracture origins leading to a reduction in the properties and reliability on the structure [3]. Each step of powder processing introduces possible defects in the structure, out of which many of the detrimental heterogeneities arise from the powder itself, such as agglomerates and contamination. Microstructural heterogeneity and flaws in ceramics fabricated by dry pressing is associated with organic and inorganic inclusions from binders and dissolved salts in the dry powder [3].

Higher quality ceramics with fine grains and minimal porosity require fine powders and uniform high-density packing. The reduction of inhomogeneity in microstructure and defects with better control over interparticle interaction to produce dense green bodies, is possible by dispersed suspensions through colloidal processing [4]. Only colloidal processing can accommodate the integrated use of homogeneous mixture of ceramics, polymers, macro-molecules or solvents, and tailoring of interaction forces between particles for the fabrication ceramics with intentional porosity [5].

1.1. COLLOIDAL PROCESSING OF CERAMICS

A colloidal dispersion is a multiphase system in which one phase (within the nanometer (10^{-9} m) to micrometer (10^{-6} m) range) is dispersed in a continuous medium. The ceramic suspension for colloidal processing involves dispersion of powders in liquids, either for direct consolidation (as in casting processes, gel forming, etc.) or as an intermediate step for further processing [6].

According to, DLVO theory the stability of colloidal suspension is governed by the balance between the attractive van der Waals force (V_A) and repulsive electrostatic double layer force (V_B) [7]. The overall net interaction energy (V_T) curve plotted against the distance between the particles (D), as shown in Figure 1.1, has three characteristic features. An energy maximum whose magnitude is related to the Hamaker constant, surface potential and ionic strength, provides the energy barrier (E_B) required for well dispersed or stable colloidal suspension [8]. The primary minimum where the particles come into contact with each other leads to a coagulated colloidal suspension that can hardly be redispersed. At larger separation distance, the repulsive force vanishes resulting in an unstable flocculated suspension that can be easily dispersed.

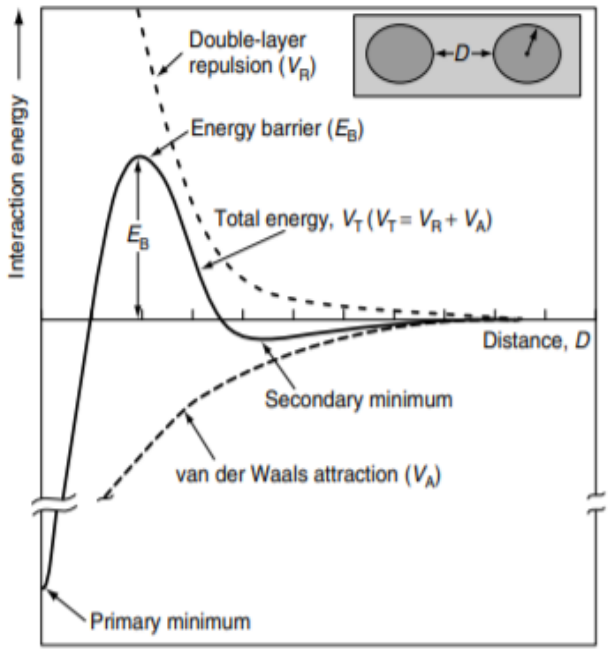

Figure 1.1. The schematic variation of interaction energy (V_T) as a function of distance separating the particles (D) according to DLVO theory [9].

Well dispersed suspensions are preferred for colloidal processing over flocculated suspensions as they retain the microstructural integrity after drying without shape deformation. Adjusting the pH of colloidal suspension or increasing the ionic strength potentially renders the suspension unstable [10]. However due to the recent developments in sensing apparatus, other forces such as short-range hydration force, long-range hydrophobic force, bridging and steric forces have been reported. Additives alter the action of these interaction forces to produce stable zirconia (ZrO_2) suspensions as observed by Leong et al. [11] through yield stress measurement using vane rheometer.

During the 1930s, colloidal processing was used in producing ceramics for advanced applications such as low-density refractory material for handling highly pure molten metal.

Thompson et al. [12], used slip-casting to fabricate thin-walled crucibles of Al_2O_3, silicon carbide (SiC) and ZrO_2 from aqueous suspensions. Later in the mid- 1940s, significant advancement in colloidal processing occurred when Howatt et al. [13], developed titanium dioxide (TiO_2) thin films through tape casting for use as capacitors. Tape-casting has become a processing technology used around the world commercially, to manufacture electronic and structural ceramics with thicknesses typically ranging from 25 to 1000mm.

In 1960-70s the knowledge of colloidal particle interactions was incorporated into processing of advanced ceramics with focus on oxides and SiC [45]. In 1980s concepts from surface chemistry (such as surface forces) and suspension rheology were incorporated into powder processing of advanced ceramics leading to the development of techniques such as injection molding [12], direct coagulation casting (DCC) [13] and freeze casting [14] in addition to the traditional colloidal shaping processes of ram pressing, jiggering, extrusion, slip casting, and tape casting. Solid freeform fabrication (SFF) of ceramics originally developed for rapid prototyping, is a novel method with potential of producing complex ceramic components with locally controlled composition and structure. SFF techniques include three-dimensional printing (3DP) [15], robocasting [16], stereolithography [17], and fused deposition [18].

Colloidal processing provides the ability to consolidate the desired porous structure and form it into any complex desired shape. Porous ceramics are of significant interest due to their wide applications as filters and membranes for separation [19], engineered thermal and acoustic insulation [20], biological implant materials [21] and solid oxide fuel cells (SOFCs) [22].

Many porous ceramics including alumina (Al_2O_3), barium titanate ($BaTiO_3$) and TiO_2, with desired microstructure and pore morphology are fabricated. The techniques involved in colloidal synthesis of porous ceramics utilize organic compounds which self-organize based on the

interactions with the inorganic components. The resulting composites are then either calcined or chemically etched, yielding porous replicate with periodic voids [23]. The organics used in the manipulation of pore morphology does not yield monomodal pore size and leave an imprint even after they disappear after sintering [24].

Research into soft matter science has impacted the colloidal processing of ceramics not only through better understanding of the effect of organic additives, but also in exploiting new mechanisms to control the assembly of suspended particles using external fields [25]. Following the earlier studies on the effect of external fields on the phase behavior and assembly dynamics of colloidal ensembles, attempts have been made to utilize external fields as means to control the assembly of ceramic particles into tailored microstructure [26]. The use of external fields to control the microstructure of ceramic parts enables unique alignment and configurations beyond what can been typically achieved using the shear forces often applied in ceramic manufacturing processes like tape casting and extrusion [27].

1.2. EXTERNAL FIELD INDUCED PARTICLE MANIPULATION

The effective and controlled manipulation of micro / nano particles is employed for a wide range of scientific and industrial applications such as drug delivery, microfluidic lab-on-chip, and self-driven micro-robots in fuel solutions [28]. The techniques for particle manipulation are classified into two categories: contact/ passive and contactless/ active [29]. The passive mode utilizes the interaction between particles, between particles and microchannel structure and particles and flow [30]. Active/ contactless mode of particle manipulation involves applying external field to control the particles.

Low- Reynolds number hydrodynamic effect employed in several contact/ passive particle manipulation methods presumes that the particle centers will follow the flow at low *Re*. Figure 1.2

(a) shows the working principle of pinched flow fractionation (PFF) which utilizes the concept of laminar flow profile inside a microchannel for continuous size separation. In PFF, the suspension of particles with different sizes is introduced from Inlet 1, and liquid without particles is introduced from Inlet 2. Particles are made to align with Sidewall 1 regardless of their sizes by tuning the flow rates at the pinched segment, causing a difference in the center positions of large and small particles. In a sudden expansion at the downstream, the particles with different sizes are separated relative to sizes by spreading flow profile into branched segments [31]. More precise separation can be achieved when the number of the branch channels is increased, or when the pinched segment is narrowed.

Hydrodynamic filtration shown in Figure 1.2 (b), works on similar operating principle. This method achieves continuous particle separation and concentration at multiple perpendicular branches from a suspension introduced into the main segment. The size of the arrows represents the magnitude of flow rate at the branch segments. At low flow rate portion of fluid is withdrawn from the main stream; whereas when the flow rates distributed into the side channels are increased, particles near the walls go through the branched channels. This technique requires precise microchannel fabrication to finely control the velocity profile and flow rate ratio at the branch point according to the cut-off size of the filtered particles [32].

The passive/ contact techniques are prone to cause physical and chemical damages to the particles and the medium in which they are suspended due to direct contact and addition of auxiliary materials to increase the effectiveness of the manipulation techniques. Therefore, label-free contactless techniques such as optical fractionation, dielectrophoresis, magnetophoresis etc., are preferred to overcome the challenges of passive mode of particle manipulation. An external field is effective not only for particle separation but also for its manipulation which includes not

only trapping, but also transportation, patterning of particles and evaluation of physiochemical properties and interactions that occur on the particle [33].

The active/ non- contact based particle manipulation techniques for involve control over particle interactions and alignment in the suspension by integrating externally applied energy fields such as optical, acoustic, magnetic and electric. Combining external energy field with colloidal processing techniques, such as slip casting, freeze casting, and additive manufacturing, is used to manipulate the microstructure over different length scales and produce texturally aligned green body [34].

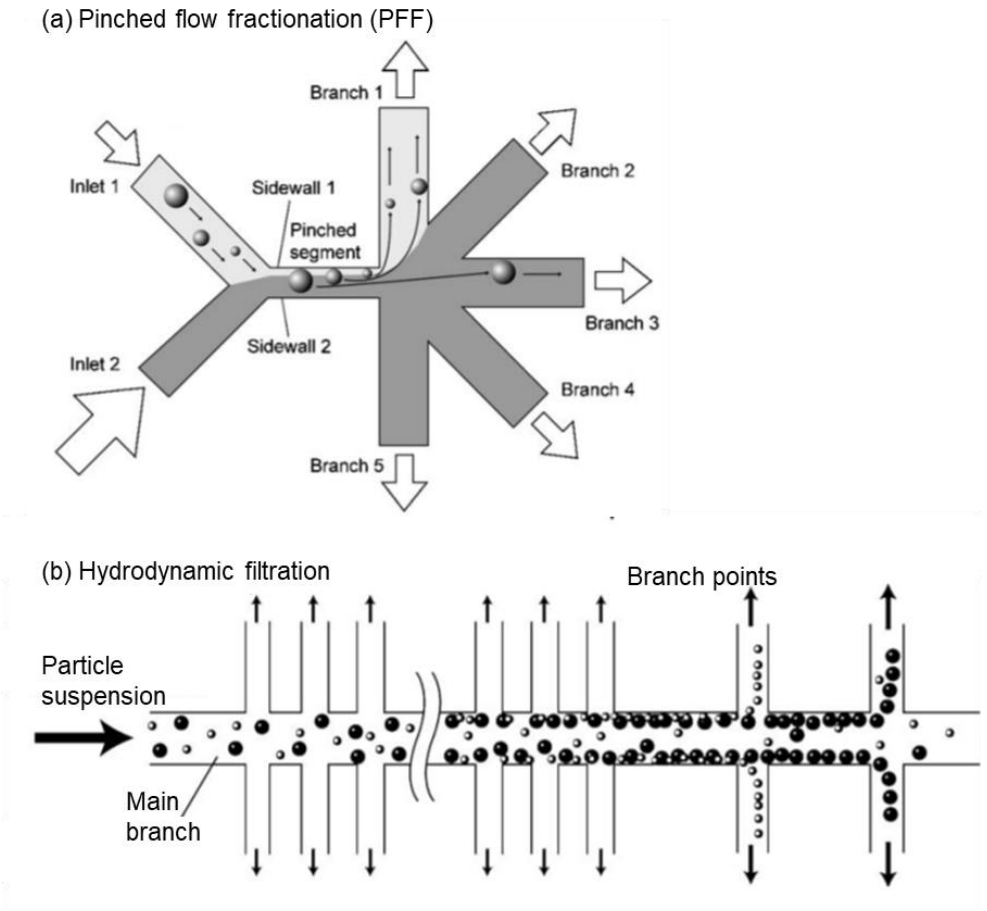

Figure 1.2. Principle of (a) pinched flow fractionation (PFF) and (b) hydrodynamic filtration. The size of the arrows represents the magnitude of flow rate.

An optical field attracts particle with refractive index higher than the medium to the center of the laser beam [41], as shown in Figure 1.3 (a) where the yellow shaded area represents the active optical field generated by the light beam captured between ITO substrate and black arrow represents the direction of force generated on the particle. This technique is particularly suitable for the trapping and manipulation of a single particle or cell. Niu et al. [35], applied optical field through laser beam to fabricated (Al_2O_3-ZrO_2)/Y_2O_3 eutectic ceramics without using any binders by laser engineered net shaping technique. However, high powered laser used to overcome the high viscosity and low photosensitivity of the suspension may cause cracks and other defects. Despite being a powerful tool for spectroscopy and biomolecular manipulation, optical field is limited to particles with larger size, media with high refractive index and suffers from complicated optics set-up [61].

As opposed to optical field, acoustic field manipulation can be performed in a variety of media, such as gas, aqueous solutions, and organic solvents. This is a good contrast to other physical fields, which often require special properties of media for successful particle manipulation [34]. Alternating nodes and anti-nodes are created on the standing acoustic wave between the transducer and reflector set-up, as shown in Figure 1.3 (b), the acoustic force moves the particles towards nodes/ anti-nodes depending on the difference between particle and medium density. However, acoustic field suffers from similar set-up related drawbacks as the optical field. The acoustic radiation force is proportional to the particle size rendering the acoustic field manipulation inapplicable to nanoparticles [36]. Ice-templating process in conjunction with acoustic radiation force, known as ultrasound directed assembly, was used to create freeze cast TiO_2 scaffolds with alternating dense and porous regions [37].

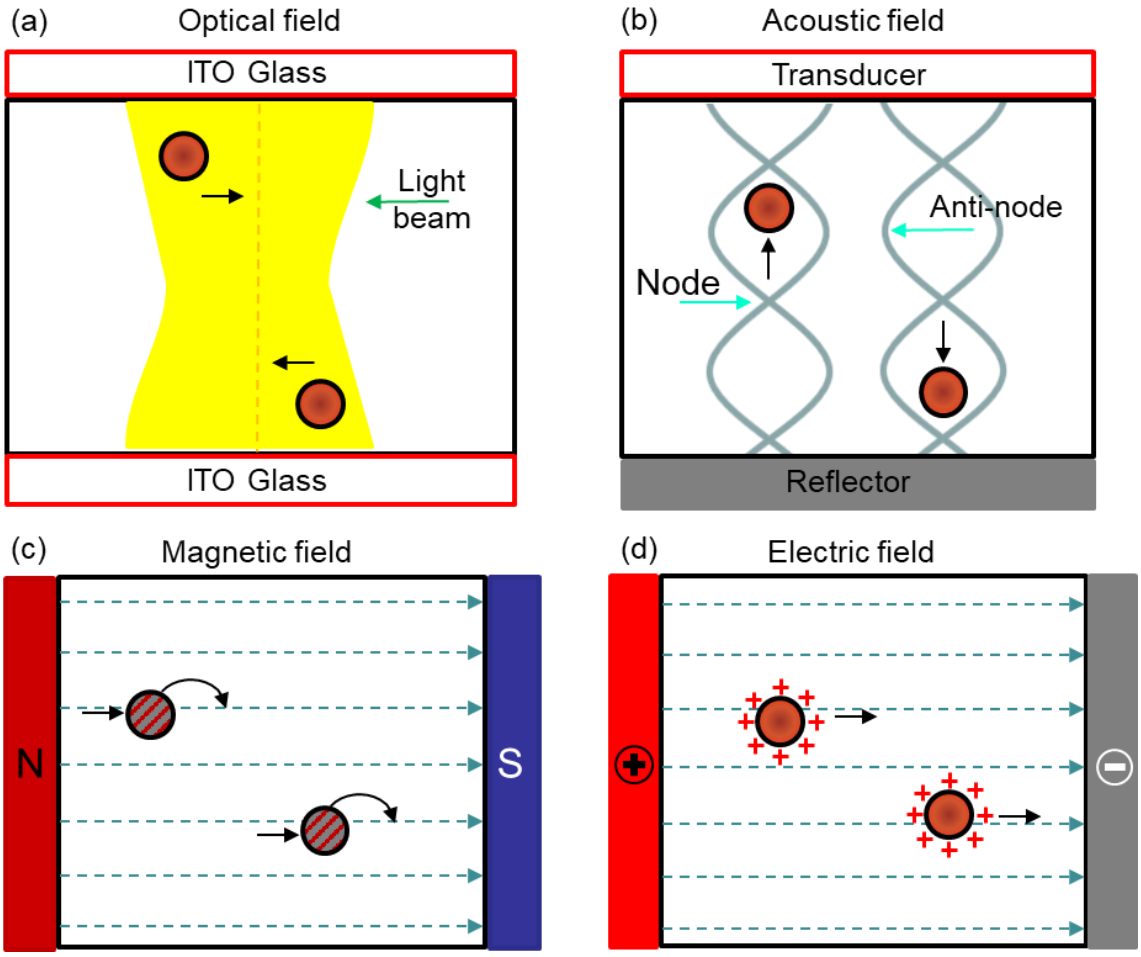

Figure 1.3. Particle motion induced by external field application. The direction of net force is shown by black arrow.

The magnetic field because it acts over a large distance, is suitable for the separation and manipulation of multiple magnetic particles and ferrofluid. Magnetic field offers a versatility to be coupled with multiple ceramic processing techniques like slip casting, ice- templating and tape casting, to orient anisotropic particles, as shown in Figure 1.3 (c). Direct magnetic particle manipulation is straightforward, but it requires strong magnetic field gradients so that the effective

local working space is small, and it requires functionalized magnetic particles limiting its applications in ceramics which are predominantly diamagnetic [38]. Sato et al. [39] presented a fabrication method for textured Ti_3SiC_2 ceramics by slip casting in strong magnetic field to enhance the bending strength and fracture toughness.

Electric field-driven particle manipulation may be the most popular and versatile technique because of its general applicability and adaptability as well as the ease of operation and integration into lab-on-a-chip systems [40]. The two major phenomena observed as a consequence of applied electric field are Electrophoresis (EP) and Dielectrophoresis (DEP). Electrophoresis (EP) is the movement of an electrically charged surface relative to a stationary liquid, induced by an applied electric field, as shown in Figure 1.3 (d). This effect can be used to transport, sort, or trap charged particles within a liquid with relatively low conductivity [41]. The rapid response, easy device construction and high reproducibility favors electrophoresis to be used in electrophoretic displays, fabrication of TiO_2 thin films by Electrophoretic Deposition (EPD) etc. [42]. A wide range of thin films, ceramic laminates and coatings are fabricated by electrophoretic deposition (EPD) which utilizes the movement of charged particles relative to stationary fluid when electric field is applied.

Ceramics fabrication through EPD are prone to non-uniformity in the deposited layers and delays when substrates with low conductivity are used, which is demonstrated in fabrication of yttrium-stabilized zirconia thin films on $L_{0.9}Sr_{0.1}MnO_3$ substrate [43]. Sedimentation of large particles, flocculation of unstable suspensions and joule heating of the fluid medium especially near the electrodes limit the applicability of electrophoretic deposition [44]. Dielectrophoresis (DEP) allows in situ structuring of ceramic particles in composites via directed self-assembly, offering a simple alternative to more complex procedures like ultrasonic cutting, injection molding, laser machining, co-extrusion, tape-lamination and fiber insertion [45].

1.3. DIELECTROPHORESIS

Dielectrophoresis (DEP) has emerged as an important technique for the manipulation of micro- and nano-sized particles in recent years. The dielectrophoretic force experienced by the particles is useful in extensive manipulation of dielectric particles which find applications in concentration, separation, sorting, and transportation for micro/nano-sized cells, protein, DNA, and particles with high aspect ratio [46]. The dependence of DEP force on the dielectric properties and particle size is exploited for filtration of metallic, ceramic and plastic particles from non-conductive medium at high flowrate, air-conditioning test dust and PVC particles from oil [47]. The dielectrophoretic microfluidic devices operate based on the intrinsic electrical properties of the particles and do not involve moving parts thereby offering efficient handling over some of the traditional techniques. For instance, new class of microwires were fabricated from suspension of metallic nanoparticles using dielectrophoretic assembly [48], 3D stem-cell scaffolds were produced by aligning graphene with PEG hydrogel by using platinum electrodes on glass substrate [49] etc.

Dielectrophoretic phenomenon arises when polarizable particle in non-uniform electric field. The non-conducting particles are polarized when placed in uniform and non-uniform electric field shown in Figure 1.4 (a) and (b), respectively. The net force acting on the particle in non-uniform field shown in Figure 1.4 (b), is unbalanced on the polarized particle resulting in the DEP effect. The permittivity of the particles determines the polarization properties with respect to the suspended medium. The particles with higher permittivity than the medium shown in Figure 1.4 (c), the dielectrophoretic force generated moves the particle towards high electric field region known as positive dielectrophoresis (p-DEP). Whereas in Figure 1.4 (d), when the permittivity of

the medium exceeds that of the particle, the force moves the particle away from high electric field region known as negative dielectrophoresis (n-DEP).

When multiple dielectric particles are present in uniform electric field, as shown in Figure 1.5 (a), the particles experience DEP as they interact with the local spatial variation field. The Figure 1.5 (b) shows the electrostatic interactions between the polarized particles and field for particles exhibiting n-DEP in AC electric field result in the formation of particle/ pearl chains to minimize electric potential energies. The particle chaining phenomenon observed as a result of the non-uniform electric field around the particles is the basis of the DEP assembly technique [50]. Particles that are identical in their electrical permittivity form an assembly parallel to the applied electric field regardless of their sizes, shapes, and initial orientations. On the other hand, particles with dissimilar electrical permittivity (mixed p-DEP and n-DEP) form an assembly perpendicular to applied electric field regardless of their sizes, shapes, and initial positions [51]. It is shown that behaviors of interactive motion of dielectrophoretic particles are strongly affected by the difference in permittivity between the particles and the fluid medium.

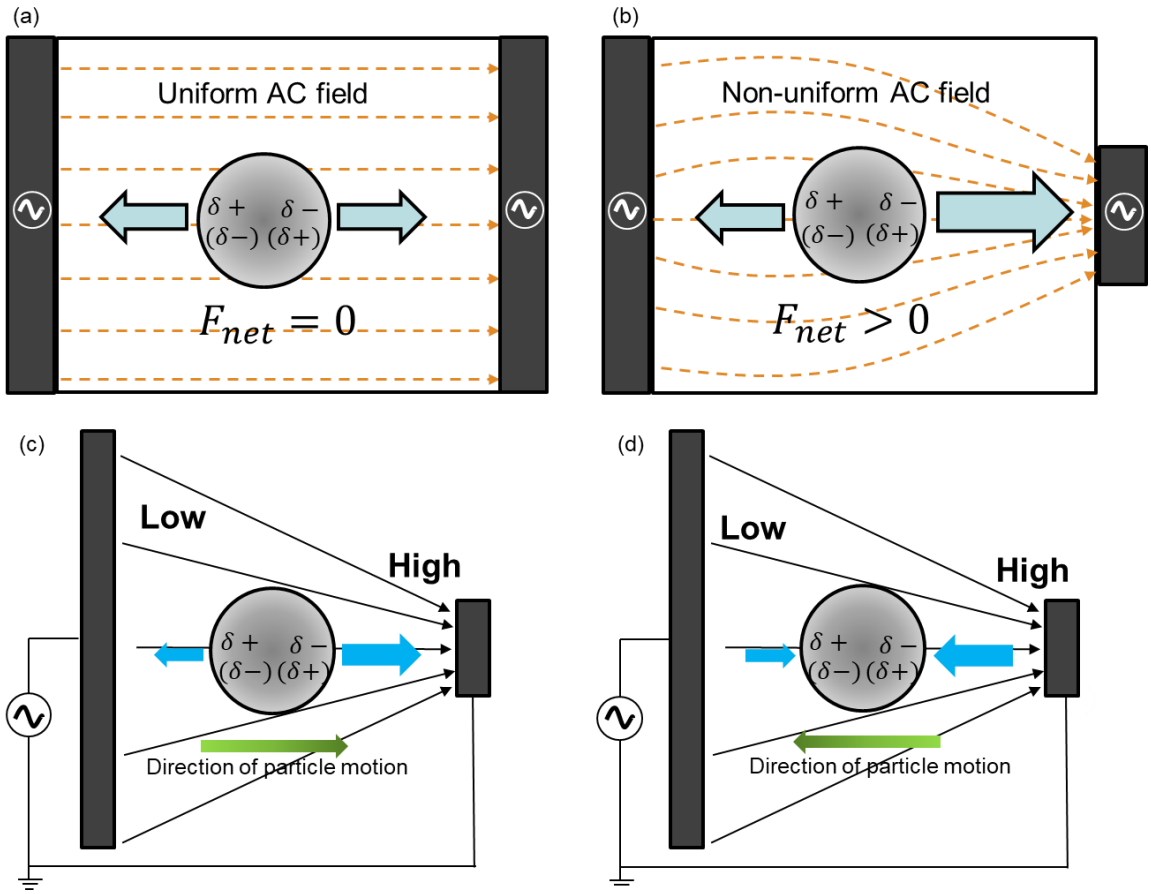

Figure 1.4. Schematic representation of polarized dielectric particle under (a) uniform and (b) non-uniform AC electric field. The difference in electrical complex permittivity causing the particle to move towards (c) high field intensity known as p-DEP and (d) low field intensity known as n-DEP in non-uniform AC electric field.

In colloidal suspension of 5 vol.% to 10 vol. % $Pb(Zr,Ti)O_3$ ceramic particles in silicone elastomer, DEP effect destabilizes the suspension inducing unidirectional agglomeration of particles into chainlike structures as reported by [52]. Field Aided Micro Tailoring (FAiMTa) technique reported by Kim et al. [53], employs AC electric field induced DEP to orient nanoclay ployamide particles and spherical silica nanoparticles dispersed in UV cured epoxy resin.

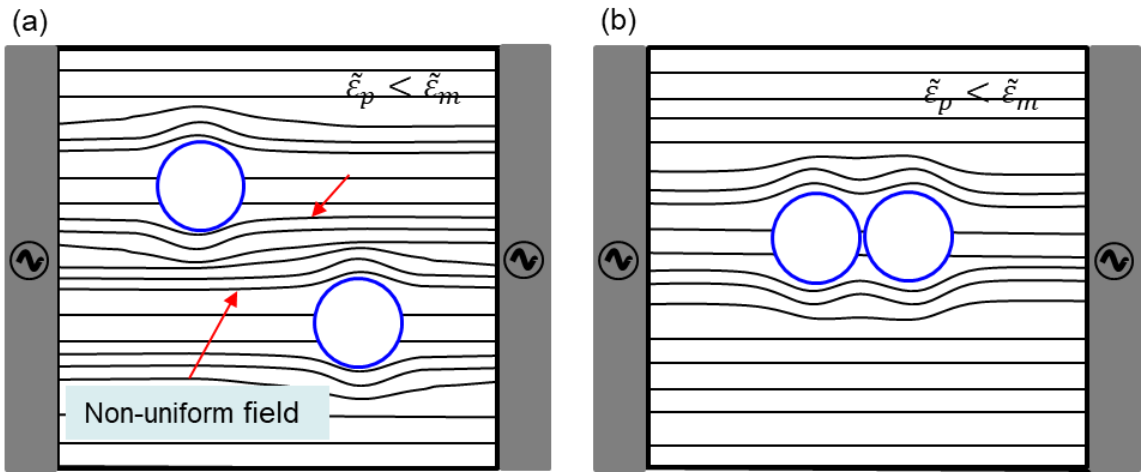

Figure 1.5. Schematic representation of particle chain formation by dielectrophoresis

In DEP the particles itself carry electrical potential and respond uniquely to the different frequencies. Whereas, in the electrophoresis technique is controlled by the particle size, density, molecular weight and purity [54]. DEP is used for particle patterning, while electrophoresis cannot create stable non-contact particle traps.

Particles in suspension have finite charge due to triboelectricity, therefore AC electric field is suitable for particle chain formation over DC field. Finite time- averaged electrophoretic force is caused only in DC field which interrupts the chain formation [55]. Applying DC field leads to electrophoresis dominating any translational DEP effect. AC electric field not only overcomes this issue for particle chain formation but also mitigates electroosmotic fluid flow and Joule heating of medium [56].

1.4. NUMERICAL ANALYSIS OF DIELECTROPHORETIC PARTICLE MOTION

The advances in DEP manipulation of particles have been facilitated by improvements in numerical techniques for solving the governing equations for the motion of fluid and particles and for electrostatic forces [57]. Numerical simulation or modelling can save resources, shorten the experimental period, and predict the motion of the particle under DEP forces therefore to optimize the design of experiments. With the rapid development of electronic computers, analytical software, such as COMSOL Multiphysics (COMSOL, Burlington, MA), computational fluid dynamics (CFD, ESI Group, France) and ANSYS Fluent (Fluent Inc, Lebanon, USA), based on various mathematical models have been widely used for the calculation of DEP forces [89].

The available software options provide accurate distribution of the electric field but in order to simulate the integrated forces of particles in a complex fluid and track the movement of particles under combined forces is challenging. Multiphysics modelling of electric field, flow field, thermal field and particle trajectories, which are characterized by coupled calculation solving flow-electricity-particle motion can correctly reveal the interactive motion behavior of the DEP particles in a uniform electrical field. The particle velocity and time behavior of interactive motion could be investigated.

Different methods have been studied to compute the forces involved, such as the effective dipole moment [60], Maxwell stress-tensor [58] and Iterative dipole moment [64]. The assumption for effective dipole moment is that the size of particle should be far below the characteristic length of the electric field. The DEP particle interaction estimated based on effective dipole moments is applicable in dilute particle conditions but inaccurate for the estimation of multiple particle interactions [59]. When the particle radius and domain size are comparable, for the estimation of

dielectrophoretic force two methods are suggested which provide solution with higher accuracy, Maxwell Stress Tensor (MST) and Iterative Dipole Moment (IDM) methods.

In the MST method, numerical integration of Maxwell stress tensors around the particle surface needs to be done. Therefore, although MST method which is considered as the most rigorous method to determine the dielectrophoretic force, it is computationally expensive and time consuming [61]. Iterative dipole moment method (IDM) that is employed in this study provides accurate interaction forces in comparison to MST method does not require solving complicated differential equations. IDM method involves calculating the interacting forces and motions of multiple dielectrophoretic particles by iteratively correcting the local electrical field.

Several studies have been performed on the numerical simulations to gain insight into the DEP particle assembly mechanism. Aubry et al [62], used point dipole method to calculate the DEP force when the particles are placed sufficiently apart in DC electric field and arbitrary Lagrange-Eulerian method to estimate the particle motion. Subsequently, Ai and Qian [63] investigated the two-dimensional DEP force on two particles present in external AC electric field to show the interaction between the particles in negative DEP results in a particle chain parallel to the applied electric field. IDM method proposed by Liu and Wu et al. [64] has been proven to be a simpler and has comparable accuracy with Maxwell Stress Tensor method. Dynamics simulation and Monte Carlo methods were used to explain the chain formation when a large number of particles were suspended in an aqueous medium. Derakhshan et al. [65] using a new solver developed in OpenFOAM to simulate the separation of three polystyrene particles provided a novel design for continuous separation of particles/cells in a two-component fluid flow by dielectrophoresis.. Research into dielectrophoretic phenomena is largely focused on bioparticles,

microfluidic devices, micro fabrication and manipulation of nanotubes with limited studies on the effect in ceramics [68, 67, 66].

To achieve effective control of ceramic particles in concentrated suspensions through dielectrophoresis, an in-depth understanding of the particle interactions in AC electric field is essential. Extensive study of the ceramic particle trajectories under DEP force due to local non-uniform electric field and relevant drag and repulsive forces based on classical Newton laws has not been carried out. In the present study, the IDM method is employed to simulate particle-particle interactions of 1024 particles in 20 vol. % aqueous suspensions in two-dimensional domain. The particle motions leading to chain formations under different material compositions and AC electric field frequency are investigated.

II. MATHEMATICAL MODEL

This chapter will cover the constitutive equations required to simulate the particle interactions subjected to dielectrophoretic, hydrodynamic and particle collision forces. The interactive motions of circular homogenous particles suspended in two-dimensional incompressible fluid medium under AC electric field are investigated where the electric double layer thickness is less than the interparticle distance. The equations listed are used to analyze the distribution of local non-uniform electric field, the force acting on the particles and describe the non-trivial trajectory solution of multiple dielectric particles under dielectrophoresis that cannot be deduced from the electric field distribution.

2.1. DIELECTROPHORETIC FORCE

In this study, Iterative Dipole Moment (IDM) method is employed to estimate the ponderomotive dielectrophoretic force exerted by local non-uniform electric field on polarizable neutral particles leading to the formation of particle chains. The DEP force estimated using Maxwell Stress Tensor (MST) method most accurately estimates the particle-field interactions in low concentrated suspensions, but then becomes computationally exhausting when multiple particle interactions are involved. Hence, for the numerical simulations to describe the effect of external AC field on the aqueous ceramic suspension involving 1024 particles, Iterative Dipole Moment (IDM) method is used, where the local electric field is iteratively corrected to estimate the dielectrophoretic force acting on the particles suspended in the domain.

2.1.1. Iterative Dipole Moment method

Consider ‘N’ neutral non-deformable circular particles suspended in a rectangular domain (L_x x L_y) containing incompressible Newtonian fluid. Figure 2.1 (a) shows the schematic

representation of the computational domain used to simulate the particle motion in the two-dimensional domain under uniform AC electric field. The rectangular domain has electrically insulated solid walls to maintain a constant volume fraction. The length of the rectangular domain is L_y and the electrodes are placed on left and right walls separated by distance L_x. In this configuration the electrodes and walls produce a repulsive force against the colliding particles equal to the dielectrophoretic force driving towards them. 2D non-deformable circular particles of diameter '2a' are suspended in the aqueous medium in a uniform pattern separated by average distance 'd' from each other and 'w' from the wall or electrode. The DEP particle motion is carried out by the AC electric field of strength $\tilde{E}$, applied along the x-axis.

Figure 2.1 (b) shows the various steps involved in estimating the converged electric field distribution to calculate the DEP force acting on particles. The first step of IDM method involves calculating the dipole moment arising from the polarized dielectric particles under the action of an external AC field. Subsequently, dipole induced electric field created by the polarized particles around the neighboring particles is estimated. Local electrical fields around multiple particles are corrected by additional electrical fields resulting from the dipole moments of the particles. The corrected field induces new dipole moment, resulting in second corrections of local fields. The field corrections can be repeatedly carried out till a convergence criterion is reached to obtain accurate local fields around all particles. The converged electric field is used to calculate the DEP force acting on individual particles.

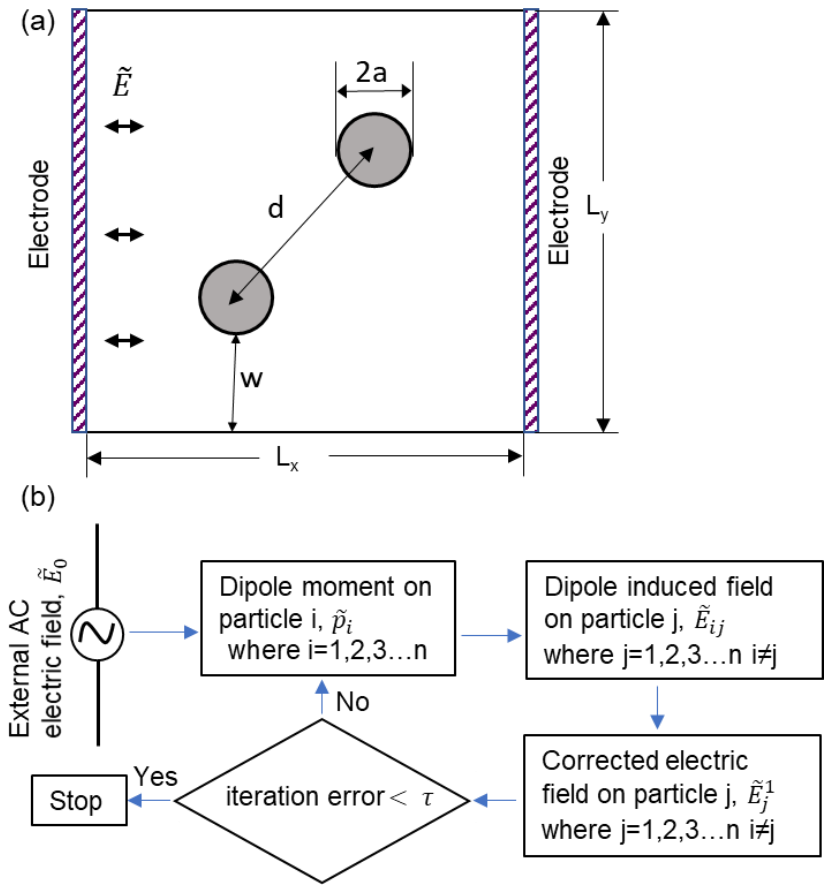

Figure 2.1. (a) Schematic of two particles arranged in a two-dimensional domain and subjected to uniform AC electric field of intensity $\tilde{E}$. (b) Flow diagram of IDM method to estimate the converged electric field on particles.

The particles acquire a polarized charge when AC electric field is applied. The induced dipole moment on the particles located at (x_i,y_i) (where i = 1,2,3…N) under uniform electric field of strength $\tilde{E}_0$ is expressed as,

$$\tilde{p}_i = 2\,\pi\, a_i^2 \varepsilon_m K_i(\omega)\tilde{E}_0 \qquad (2.1)$$

where $\tilde{p}_i$ and a_i denote the complex dipole moment and radius of the ith particle, and the superscript '~' denotes complex variables. Clausius-Mossotti factor, $K_i(\omega)$ which determines the direction of the DEP force is given by,

$$K_i(\omega) = \frac{\tilde{\varepsilon}_p - \tilde{\varepsilon}_m}{\tilde{\varepsilon}_p + \tilde{\varepsilon}_m} \tag{2.2}$$

where $\tilde{\varepsilon}_p = \varepsilon_p - j\frac{\sigma_p}{\omega}$ and $\tilde{\varepsilon}_m = \varepsilon_m - j\frac{\sigma_m}{\omega}$ are the complex permittivity of particle and fluid, respectively. ε_p and σ_p are the permittivity and conductivity of the particle, and ε_m and σ_m are the permittivity and conductivity of the medium, respectively. $\omega = 2\pi f$ is the angular frequency of the AC electric field.

The dipole induced electric field is given as,

$$\tilde{\varphi} = \frac{\tilde{\boldsymbol{p}} \cdot \boldsymbol{r}}{2\,\pi\,\varepsilon_m\, r^2} \tag{2.3}$$

$\boldsymbol{r}$ is the position vector originated from the ith particle located at (x_i, y_i), and $r = |\boldsymbol{r}|$. The additional electric field induced by the ith particle on jth particle is given as,

$$\left(\tilde{E}\right)_{ij} = \frac{-a_i^2 K(\omega) \cdot \left(\tilde{E}_{0x}(x_j - x_i) + \tilde{E}_{0y}(y_j - y_i)\right)}{r^4} \tag{2.4}$$

The corrected field $\tilde{E}_j^{(n+1)}$ as a result of the dipole induced field by the ith particle is,

$$\tilde{E}_j^{(n+1)} = \tilde{E}_j^{(0)} + \sum_{i=1, i\neq j}^{N} \tilde{E}_{ij}^{(n)} \tag{2.5}$$

where $\tilde{E}_j^{(0)}$ is the applied electric filed at the jth particle center and n denotes the iteration number [69]. The corrected field induces a dipole moment leading to a new dipole induced electric field and subsequently a second corrected field. The electric field is iteratively corrected until convergence is reached which is defined as,

$$\left|\frac{\tilde{E}_j^{(n+1)} - \tilde{E}_j^{(n)}}{\tilde{E}_j^{(n+1)}}\right| \leq \tau \tag{2.6}$$

τ is the convergence criteria of the iteration error. The time averaged 2D dielectrophoretic force resulting from the corrected filed is expressed as [70],

$$F_{dep} = \pi a^2 \varepsilon_m Re[K(\omega)] \nabla \left|\tilde{E}\right|^2 \quad (2.7)$$

2.1.2. Code validation

DEP force in two-dimensional AC electric field calculated by IDM method is compared to MST method to verify its accuracy. The particles 1 and 2 each of radius 5 μm having relative permittivity $2.5\varepsilon_0$ and conductivities 5 x 10^{-3} S/m and 0.3 x 10^{-3} S/m respectively, are suspended in fluid medium with permittivity $7.8\varepsilon_0$ and conductivity 5 x 10^{-3} S/m inside a square domain of size 100 μm x 100 μm as shown in the Figure 2.2 (a). A uniform electric field of 0.1 x 10^{-3} V/m is applied across the electrodes. The particles are located at 45° directional angle between the connecting line of the two particle centers and the electrical field (the x-axis). The variation of applied AC field frequency with the real (CMF) of the particles is shown in Figure 2.2 (b). At low frequency, the particles 1 and 2 act as p-DEP and n-DEP particles respectively, whereas at frequency over 10 MHz both particles behave as n-DEP.

The time averaged DEP forces on the particles by MST method are estimated using a refined grid to obtain grid independent numerical solution by Xie et al [70] using COMSOL Multiphysics. The converged electric field to determine the DEP force using IDM method employs convergence criterion (τ) to be less than 0.001.

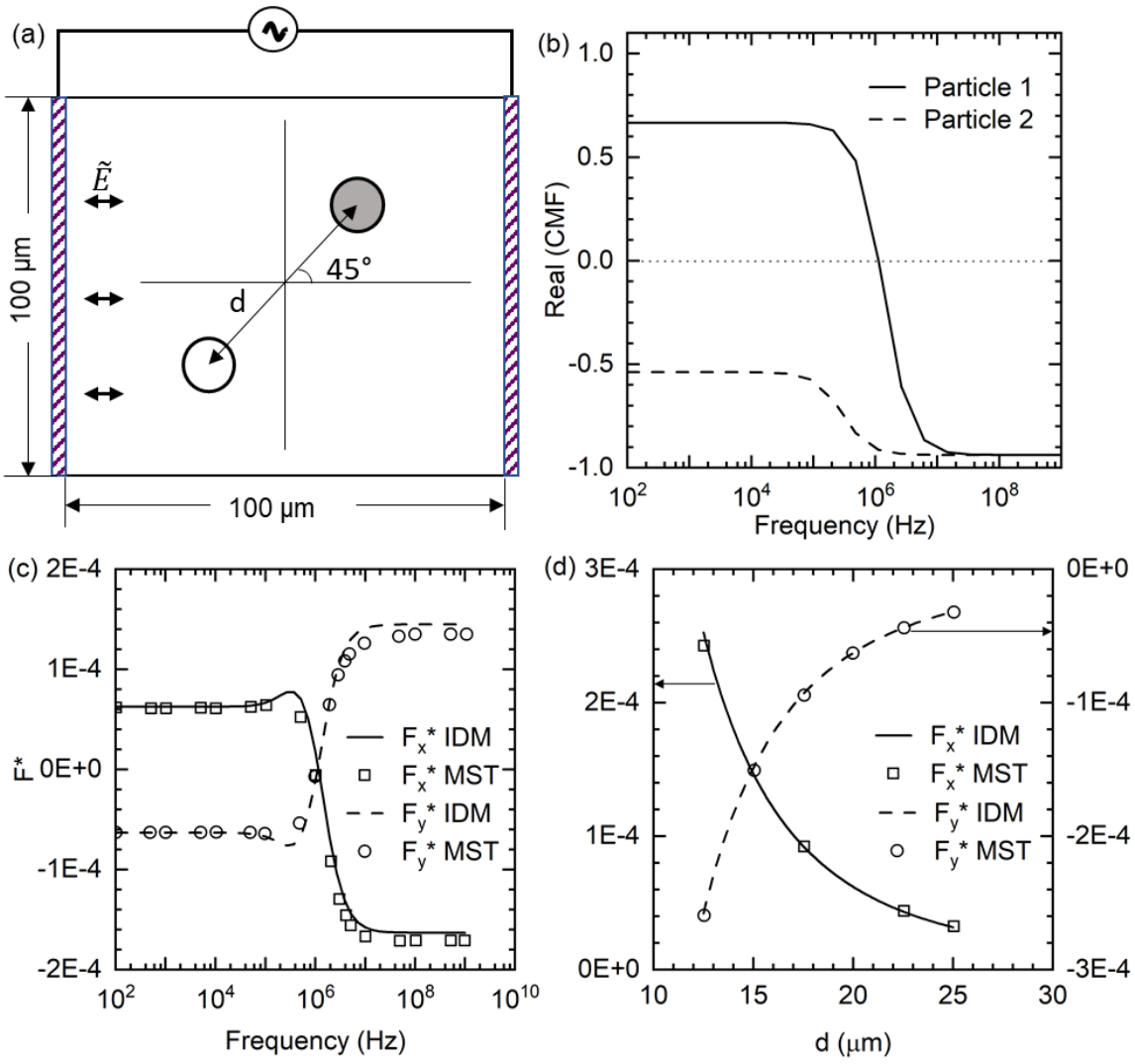

Figure 2.2**.** Validation of IDM method. (a) Particles 1 and 2 shown as white and gray circular markers respectively, separated by a distance d, are placed in domain of size 100 µm x 100 µm at an angle of 45° with the applied AC electric field ($\tilde{E}$). (b) Variation of real (CMF) with applied AC field frequency for particle 1 and 2. (c) Variation of normalized DEP force with the applied AC field frequency from 100 Hz to 1 GHz. (d) Variation of normalized DEP force in x and y directions respectively at 1 kHz with distance between particle centers by IDM method and MST method.

The DEP force normalized by the characteristic length is used to check for the accuracy of the IDM model.

$$F^{*}_{depx} = \frac{F_{depx}}{a}; F^{*}_{depy} = \frac{F_{depy}}{a} \tag{2.8}$$

where F_x and F_y are the DEP force in x and y directions respectively.

Figure 2.2 (c) shows the variation of DEP force normalized by the particle radius (5 μm), with the applied AC field frequency from 100 Hz to 1 GHz. The normalized DEP force in x and y direction (F_x* and F_y*) are estimated when the particles are separated by 20 μm, respectively. Figure 2.2 (d) shows the dependence of normalized DEP force (F*) on the distance between particles at 1 kHz AC field frequency. The dielectrophoretic force in x and y directions are shown along the left and right vertical axes, respectively. DEP force in x direction (F_x*) is represented by hollow square marker and solid line using MST and IDM methods, respectively. Similarly, DEP force in y direction (F_y*) is represented by hollow circle marker and dashed line using MST and IDM methods, respectively. It is observed that the results of IDM and MST methods are in good agreement with each other with varying distance between the particles and AC field frequency.

2.2. HYDRODYNAMIC DRAG FORCE

The hydrodynamic drag force arising from the viscous interaction of the dielectric particle and the aqueous medium is another dominant force acting on the particle [71]. The flow is governed by the Stokes equation. Stokes drag force of cylindrical particles is given as,

$$F_{drag} = \frac{16\,\pi\,\eta\,a_l}{2\ln\left(\frac{2a_l}{a}\right)-1}\,(u-v) \tag{2.9}$$

where η is the viscosity of the fluid, u is the velocity of the fluid, v is the velocity of the particle and a_l is the length of the cylindrical particle perpendicular to the two-dimensional region.

As $\frac{a_l}{a} \rightarrow \infty$, the stokes drag force exerted on the particle assuming the fluid velocity as zero is given by,

$$F_{drag} = 8\,\pi\,\eta\,v \tag{2.10}$$

2.3. REPULSIVE FORCES

The repulsive forces preventing the particles from overlapping with another particle and wall are short range spring like forces [72]. The particle-particle repulsive force is expressed as,

$$F_{rep,\ p-p} = -F_p \exp\left[\kappa_p \left(\frac{r_{ij}}{\delta_p} - 1\right)\right] \frac{r_{ij}}{|r_{ij}|} \tag{2.11}$$

The particle-wall repulsive force is expressed as,

$$F_{rep,\ p-w} = -F_w \exp\left[\kappa_w \left(\frac{w_i}{\boldsymbol{a_i}} - 1\right)\right] \frac{w_i}{|w_i|} \tag{2.12}$$

where κ_p and κ_w are constants which determines the range of the repulsive force, r_{ij} is the position vector from the center of ith particle to the jth particle, w_i is the position vector from center of ith particle to the wall, a_i is the radius of ith particle and δ_p is the minimum separation distance between the particles which is the sum of the two colliding particle radii. The spring constant, $F_p$and F_w are determined by the maximum DEP force exerted when the particles are extremely close to each other and insulating wall (~10 nm), respectively.

2.4. PARTICLE MOTION

The movement of the particles in the computational domain is governed by the Newton's equation of motion as follows,

$$m_p \frac{d^2 r_p}{dt^2} = F_{tot} \tag{2.13}$$

where $m_p = \pi\, a^2 \rho_p$ is the mass of the particle, $\rho_p$is the density of the material and F_{tot} is the sum of all forces acting on the particle,

$$F_{tot} = F_{dep} + F_{drag} + F_{rep,\ p-p} + F_{rep,\ p-w} \tag{2.14}$$

where F_{dep}, F_{drag}, $F_{rep,\ p-p}$ and $F_{rep,\ p-w}$ are DEP force, drag force, particle-particle repulsive force and particle-wall repulsive force. The position and velocity of the particles is determined by the velocity Verlet method [72] which is expressed as,

$$r_i(n+t) = r_i(n) + t\, v_i(n) + \frac{t^2}{2m_i} F_{tot,i}(n) \tag{2.15}$$

$$v_i(n+t) = v_i(n) + \frac{t}{2m_i}\left(F_{tot,i}(n) + F_{tot,i}(n+t)\right) \tag{2.16}$$

where $F_{tot,i}$ and r_i are the force and position vector of the i[th] particle. The velocity u_i and the position of the particles can be determined after every time step t.

2.5. SIMULATION SET-UP

Figure 2.3 (a) shows the initial position used for the numerical simulation of 1024 uniformly distributed ceramic particles of radius 1 μm, in aqueous medium to achieve 20 vol. % solids loading ceramic suspension in two-dimensional domain of size 126 μm x 128 μm. The zoomed in portion of top left corner of the domain in Figure 2.3 (b) and (c) show the two types of initial particle distribution with an interparticle distance of 1.67 μm and 1.69 μm (i.e., distance from particle centers 3.67 μm and 3.69 μm) for configuration A and B, respectively. The center of each column of particles is separated from each other by offset of 2 μm in direction perpendicular to electric field in configuration A and 0.5 μm in configuration B. The different configurations are used to observe the effect of initial particle distribution on the particle chain formation and to introduce additional non-uniformity in the local electric field in the initial settings while simulating homogeneous conditions.

This computational set up is employed for continuous particle tracking under the influence of external electric field, which is the dielectrophoretic force and the forces that affect the particle motion i.e., hydrodynamic force, particle-particle collision force, and particle-wall collision force.

The Brownian motions are neglected in the present work as they are negligible in short-range DEP particle-particle interactions.

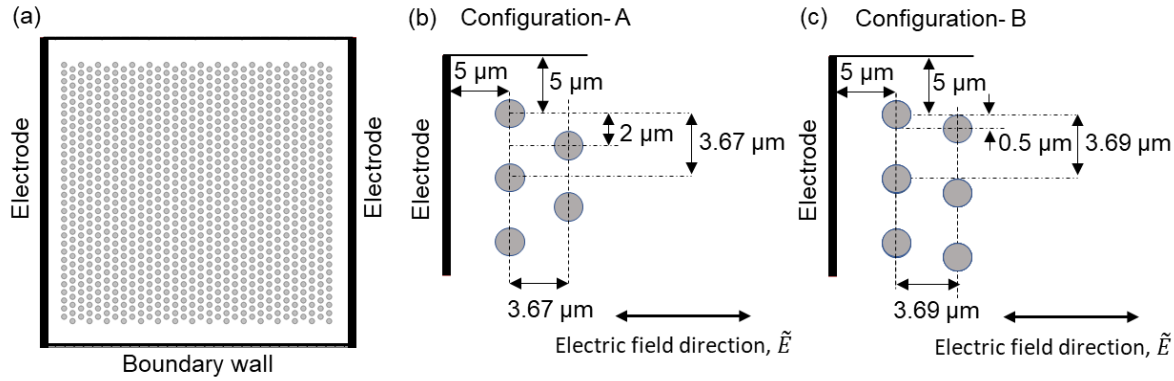

Figure 2.3. (a) Schematic showing the initial distribution of 1024 particles. The domain is bounded by electrically insulated boundary walls on top and bottom and electrodes on either side on the 2D domain of size 126 μm x 128 μm. (b) and (c) The top left corner of the 2D domain with five and six particles of configuration A and B respectively. The direction of applied electric field is shown by the double headed arrow.

Alumina (Al_2O_3) and barium titanate ($BaTiO_3$) are the two ceramic materials chosen for this study to investigate the effect of material properties [73, 74, 75, 76] on the DEP directed particle motion. Table 2.1 shows the electrical and physical properties of the ceramic materials used in the aqueous suspension. The permittivity and conductivity of the aqueous medium are $80.1\varepsilon_0$, where $\varepsilon_0 = 8.85$ x 10^{-12} F/m and 0.2 mS/m, respectively.

Table 2.1. Properties of Al_2O_3 and $BaTiO_3$

Material	**Radius (μm)**	**Density (g/cc)**	**Mass (kg)**	**Conductivity (S/m)**	**Permittivity**
Alumina (Al_2O_3)	1	3.97	0.12×10^{-6}	1×10^{-12}	$9.2\varepsilon_0$
Barium titanate ($BaTiO_3$)		6.02	0.19×10^{-6}	1×10^{-7}	$6500\varepsilon_0$

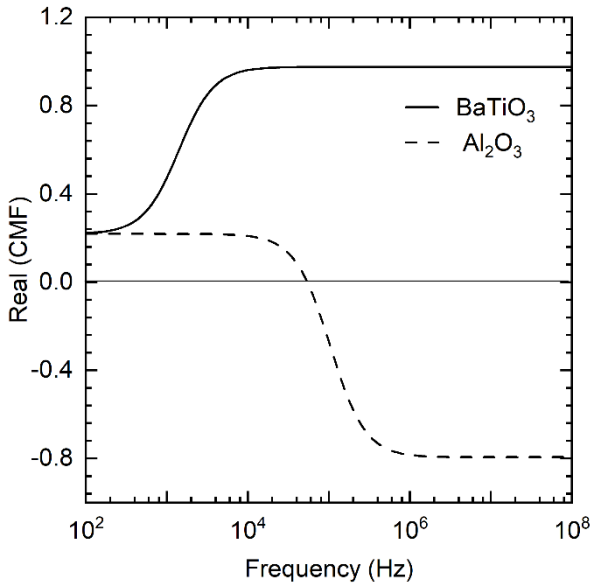

Figure 2.4. Frequency dependence of real (CMF) of $BaTiO_3$ and Al_2O_3 particles of radius 1 μm shown in solid and dashed lines respectively.

The real (CMF) of the Al_2O_3 and $BaTiO_3$ changes with the applied AC electric field frequency as illustrated in Figure 2.4. The real value of CMF over the frequency range of 100 Hz to 100 MHz is shown for Al_2O_3 and $BaTiO_3$ by dashed and solid lines respectively. Al_2O_3 exhibits p-DEP behavior at low frequency with real (CMF) value of 0.219, as the frequency increases the crossover occurs at 100 kHz turning the particles to n-DEP with real (CMF) value of -0.793. Whereas $BaTiO_3$ retains the p-DEP behavior with varying frequency. However, at low frequency the particles possess real (CMF) value of 0.221 which increases with frequency spiking at 1 kHz to 0.973 and maintained for high frequency regime.

Table 2.2 lists the dielectrophoretic particle interaction studies performed on 20 vol. % aqueous ceramic suspension and simulation conditions for each in 2D domain of 126 μm x 128 μm under applied AC electric field of 0.5 MV/m. IDM method with a convergence criterion (τ) of 0.001 is used to estimate the electric field gradient and DEP force. The numerical simulations involving single type of ceramic particles are denoted by a simulation ID beginning with 'S'. The DEP interactive motion at low electric field frequency of 1 kHz is investigated in S1 with Al_2O_3 particles initially arranged in configuration A. In S2 and S3, external AC electric field is applied to Al_2O_3 particles in aqueous suspension placed in configuration A and B, respectively at 1 MHz frequency. The influence of high frequency on the DEP particle interaction is studied on $BaTiO_3$ in S4 and S5 where the particles are located in configuration A and B, respectively.

Al_2O_3 and $BaTiO_3$ are used for the mixed particle type simulation which are denoted by a simulation ID starting with 'M'. Equal number of particles of Al_2O_3 and $BaTiO_3$ (512 each) are employed in M1 and M2, arranged in configuration A and B, respectively. The impact of p-DEP and n-DEP particles in the suspension at 1 MHz frequency on the particle chains can be observed from M1 and M2. The simulations with ID beginning with 'N', the suspension contains unequal

number of p-DEP and n-DEP particles under external AC field at 1 MHz frequency. n-DEP and p-DEP rich ceramic suspensions of 1024 Al_2O_3 and $BaTiO_3$ particles at a composition of 4:1 and 1:4 is used in N1 and N2, respectively.

Table 2.2. Simulation details of DEP particle interaction simulation on 20 vol. % aqueous ceramic suspension

	Simulation ID	**Material**	**Number of particles**	**Configuration**	**Frequency**
Single material	S1	Alumina	1024	A	1 kHz
	S2			A	1 MHz
	S3			B	
	S4	Barium titanate		A	
	S5			B	
Double material	**Simulation ID**	**Material**	**Number of particles**	**Configuration**	**Frequency**
	M1	Alumina and Barium titanate	512 (Al_2O_3) and 512 ($BaTiO_3$)	A	1 MHz
	M2			B	
	N1		204 (Al_2O_3) and 820 ($BaTiO_3$)	B	
	N2		820 (Al_2O_3) and 204 ($BaTiO_3$)	B	

2.5.1. Simulation considerations

Figure 2.5 shows the variation of DEP force and repulsive forces with the distance when only two ceramic particles are placed in the two-dimensional domain described in the previous section. The DEP force acting on $BaTiO_3$ is higher than Al_2O_3 at 1 MHz and 1 kHz as shown by the dashed, dotted and solid lines, respectively in Figure 2.5 (a). DEP force acting on particles decreases and reaches a negligible value when the particles are farther than 15 μm. Therefore, the dielectrophoretic effect on neighboring particles whose distance exceeds 15 μm is neglected for the estimation of dipole induced electric field to save computational time. Figure 2.6 (a) shows the Al_2O_3 particle distribution in M2 simulation to illustrate the range of dielectrophoretic effect of a particle taken into consideration in the numerical simulation for the estimation of converged electric field. The zoomed in portion of the 2D domain show in Figure 2.6 (b) represents the computational region of 30 μm in diameter highlighted around a particle.

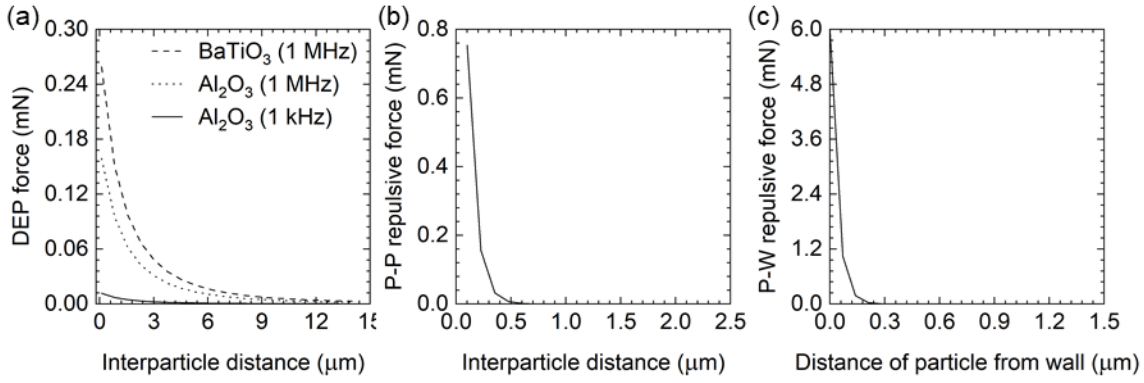

Figure 2.5. (a) Variation of DEP force with the interparticle distance between two ceramic particles. (b) Variation of P-P repulsive force between two $BaTiO_3$ particles with the interparticle distance. (c) Variation of P-W repulsive force between $BaTiO_3$ particle and the boundary wall with the distance between the particle and the wall.

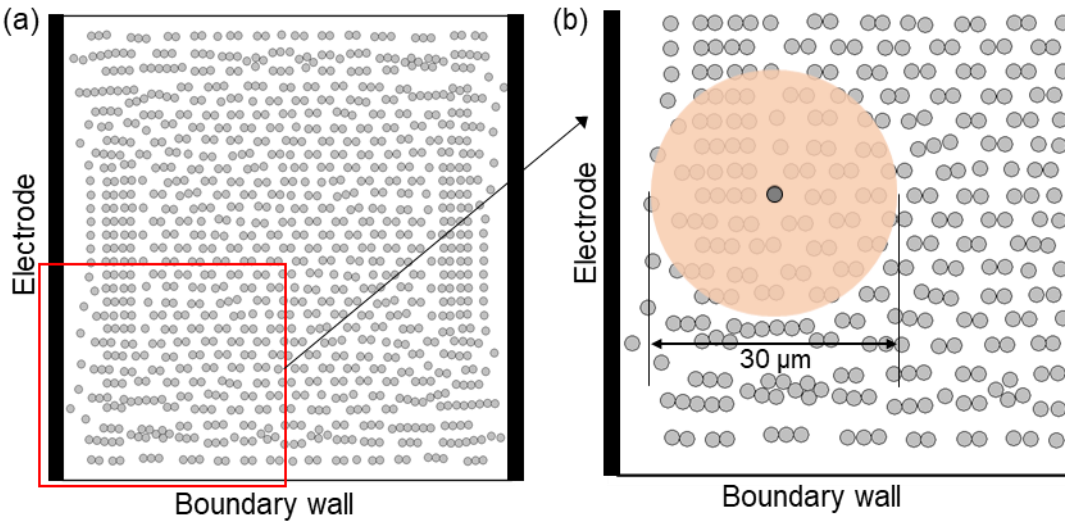

Figure 2.6. (a) Al_2O_3 particle distribution at t= 15 ms in S2 simulation. (b) The zoomed in portion of the 2D domain showing the range of dielectrophoretic effect taken included in the estimation of corrected electric field for the highlighted particle.

Figure 2.5 (b) and (c) show the variation of the short-range particle-particle (P-P) repulsive force and particle-wall (P-W) repulsive force two $BaTiO_3$ particles and between $BaTiO_3$ particle and wall with the distance from the particle. The F_p and F_w are chosen as 0.9 mN and 10 mN, respectively. The constants specifying the range of P-P (κ_p) and P-W (κ_w) repulsive forces are selected as 40 and 50, respectively. The exponential increase in the repulsive forces poses a threat of particle overlap in the simulation. Variable time step is used to calculate the subsequent position of the particles since the DEP and repulsive forces depend on the particle proximity with the neighbors. Therefore, the time step chosen for particles that are isolated and away from a particle chain is much higher compared to the particles which are part of a chain to prevent particle overlap in the simulation.

MATLAB 2019a is employed to estimate the converged electric field acting on the particles, dielectrophoretic force arising from the local non-uniformity in the electric field, hydrodynamic and repulsive forces and subsequent particle velocities and positions. However, the computational resources required for the numerical simulations involving 1024 particles is exceeds the personal computer capabilities. Therefore, internet based high performance computing cluster offering greater computational power is utilized to reduce the computational time. All cluster computations are done on a 16 node-cell on Wahab cluster (Intel(R) Xeon(R) Gold 6148 CPU @ 2.4GHz) at Old Dominion University. The input and output parameters from the HPC cluster are written to/read from text files which is later processed on MATLAB platform.

2.6. PARTICLE PACKING ANALYSIS:

The particle arrangement at the end of simulation is analyzed to extract conclusions on the characteristics of the distribution. In order to assess the particle packing, the two-dimensional domain is divided into smaller areas associated with each particle. Voronoi tessellation is a method to describe the subdivision of space by drawing straight boundaries equidistant between neighboring particles, to form polygonal cells [77]. Voronoi partition provides the geometric properties of the domain that can be used to calculate the overall properties of the particle distribution, local clusters and their neighborhood.

The Voronoi entropy calculated from the Voronoi diagram is used to quantify the orderliness of sets of points on 2D plane in material science and surface science such as grain growth and self-assembly of colloidal particles [83]. The distribution of void space and geometrical characteristics of Voronoi cells and their impact on flow distribution, pressure drop, heat and mass transfer have been studied by Haughey et al. [78] on packed bed of spherical

particles. Modelling of porous media and membranes have been performed with the assistance of Voronoi diagrams [79].

A Voronoi tessellation or diagram is a partitioning of the plane into regions based on the distance to a specified discrete set of points (particle centers) called seeds, sites, nuclei, or generators [80]. Each nucleus is surrounded by a polygonal cell whose boundaries are defined by perpendicular bisectors of lines joining a given nucleus with its nearest neighbors. The Voronoi diagram divides a region into space-filling, non-overlapping convex polyhedra [81], as shown in Figure 2.7 (b), for 1024 particles of equal size positioned in configuration A in Figure 2.7 (a). Particles that share faces of their respective Voronoi cells are called geometrical neighbors.

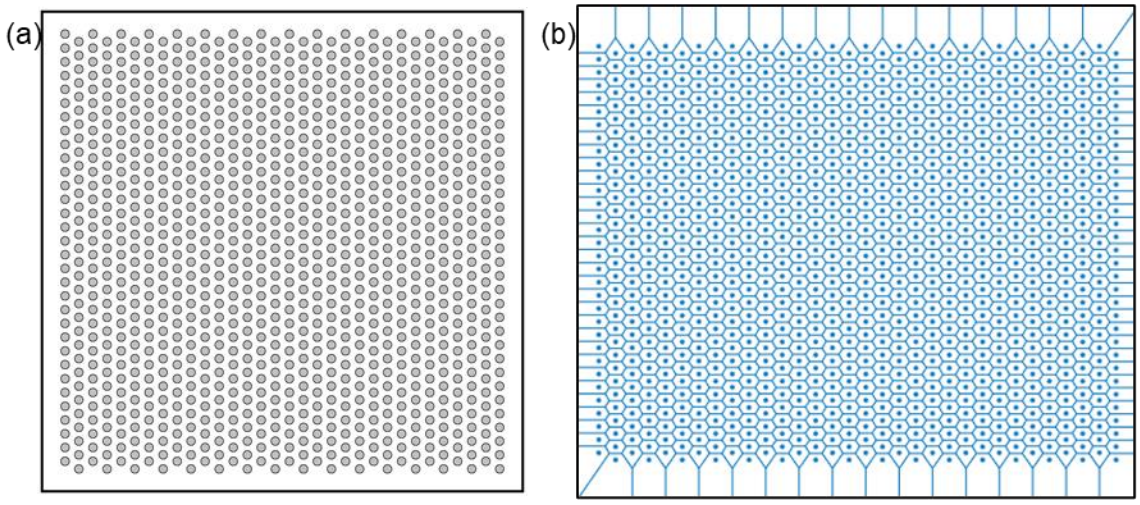

Figure 2.7. Particle packing analysis using Voronoi tessellation. (a) 1024 particle placed in configuration A. (b) Voronoi diagram of the 2D domain with the particle centers as nuclei.

The average number of geometrical neighbors independent of the randomness and density of packing calculated from a Voronoi diagram is six [84]. The geometrical neighbors of particles

located at the edges of the domain is lower than the particles located in the interior [82]. The particles that are isolated in the middle of the domain have greater number of geometrical neighbors compared to those in close ordered packing. Therefore, random sparse packing of particles will have a higher number of average geometrical neighbors than a dense packing of particles.

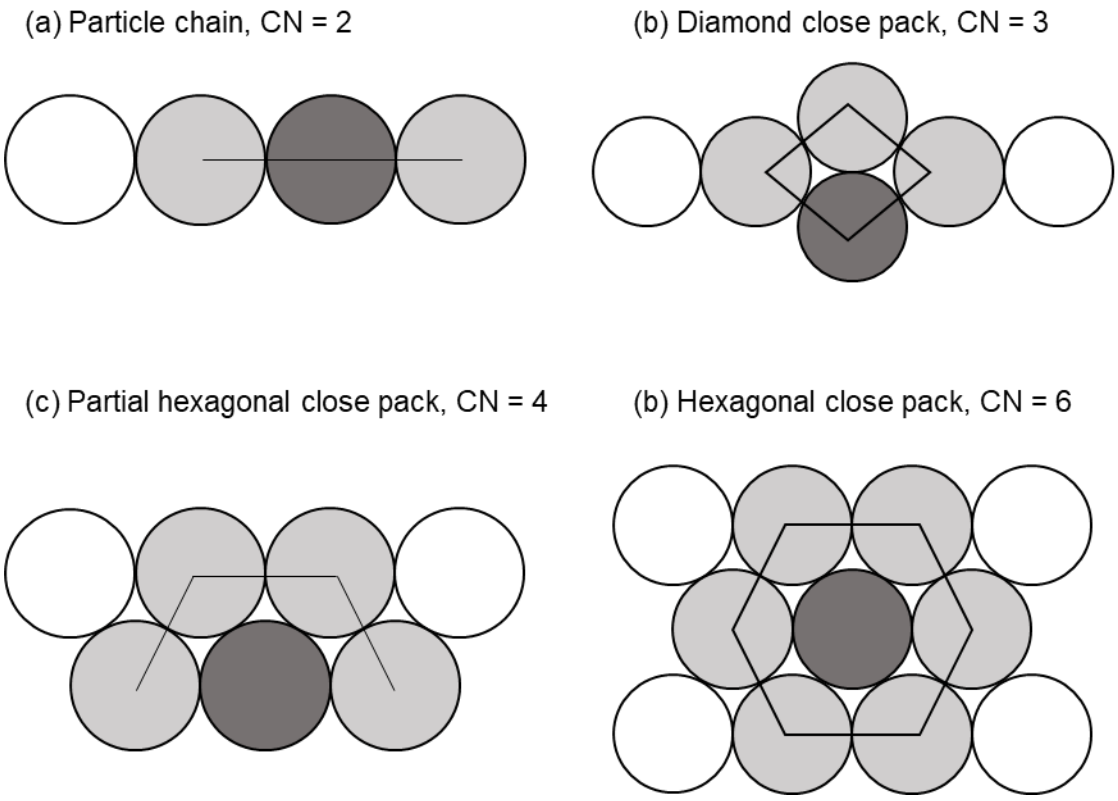

Figure 2.8. The different local particle cluster arrangements in the ceramic suspension. The particle arrangement along with the CN of highlighted particle in dark gray is shown for (a) particle chain, (b) diamond close pack (c) partial hexagonal close pack and (d) hexagonal close pack arrangement.

The structural neighbors of a particle are contained in its geometric neighbors and are those particles in contact with it. The number of structural neighbors is called coordination number (CN) [82]. The average coordination number (CN_{avg}) describes the dense packing of the particle distribution. The particles in different local arrangements that are observed in the simulations shown in Figure 2.8. The CN is estimated of particle highlighted in dark gray and the corresponding structural neighbors are highlighted in light gray. The particle chains that are aligned parallel or perpendicular to the field shown in Figure 2.8 (a), has CN of 2. Diamond close pack arrangement of particles is prominent in low frequency simulations is presented in Figure 2.8 (b) has CN of 3. In high frequency simulations the particles are mostly packed in partial hexagonal close pack arrangement with CN of 4 as demonstrated in Figure 2.8 (c). The CN of ordered densely packed particles is 6 as shown in Figure 2.8 (d), where the particles are in hexagonal close pack arrangement [83].

The structural neighbors "park" on the circumference of a particle and each one has an associated structural neighbor angle [84]. The orientation of the line joining the centroid of structural neighbor pair with the direction of electric field provides a deeper understanding of particle packing in the domain. The distribution of the angular orientation of structural neighbors gives the type of ordered packing that dominates in the domain. The structural neighbors in parallel and perpendicular chains make an angle of 0° and 90°, respectively. Whereas those in partial hexagonal close pack and hexagonal close pack arrangement are oriented at ±60° with the electric field direction.

III. RESULTS

3.1. PARTICLE INTERACTION IN LOW CONCENTRATED SUSPENSIONS

In this section, the multi-physics model was employed to investigate the relative motion of particles arising from the DEP particle–particle interaction under AC electric field, hydrodynamic drag force and particle repulsive force against the walls and each other. Validated IDM method is used to estimate the force arising from the local non-uniform electric field solely induced by the presence of particles when AC electric field is imposed across the electrodes. The computational model is initially tested on two and five ceramic particle suspensions. The range constants (κ_p and κ_w) and time step to estimate the short-range repulsive forces and subsequent position of the particle due to the forces acting on it, respectively, were verified in the simulation of the computational model with two and five particle suspensions. The data acquisition and analysis performed for the low concentrated ceramic suspension helped prevent scalability issues that arise with large number of particles in concentrated suspensions.

The initial particle distribution in the two-dimensional domain for the two and five particle simulations is shown in Figure 3.1 (a) and (b), respectively. The particles with an identical size of 1 μm radius are suspended in aqueous medium ($\varepsilon = 80.1\varepsilon_0$ and $\sigma = 2e^{-4}$ S/m) [85]. AC electric field of magnitude 0.5 MV/m at a frequency of 1 MHz is applied across the electrodes parallel to x-direction. The markers represent the particle location. The white and gray markers indicate the position of Al_2O_3 and $BaTiO_3$ particles, respectively in the simulations involving mixed type of particles.

The mathematical model is first tested on two ceramic particles in a square domain of size 12 μm x 12 μm, where the particles are placed 3 μm away from the nearest boundary wall/ electrode

and the line joining the centers are aligned at 45° with the direction of the electric field. The particles are separated by 7.07 μm, located at (2.5, 2.5) μm and (-2.5, -2.5) μm as shown in Figure 3.1 (a). The model is then tested on five particles separated by an average distance of 3.8 μm from each other and 5 μm away from the nearest boundary wall/ electrode similar to the conditions of 1024 particles in simulations S3, S5, M2, N1 and N2 in configuration B. The particles are located at (2, 2), (-2, -2), (3.25, -3.25), (-3.25, 3.25) and (0, 0) μm in a square domain of size 18 μm x 18 μm as shown in Figure 3.1 (b).

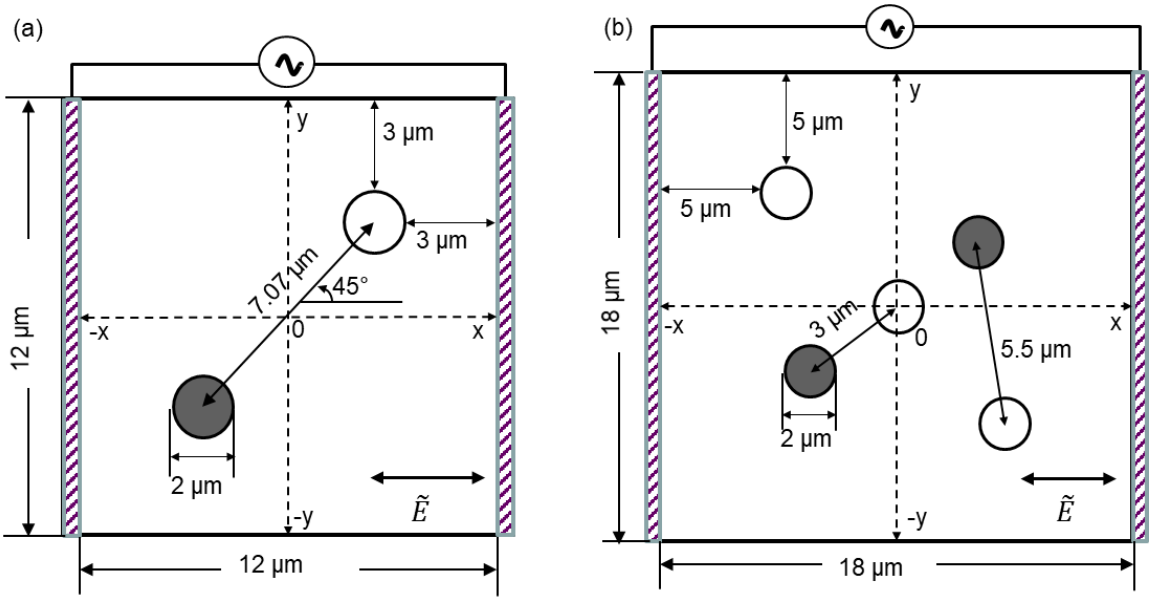

Figure 3.1. The initial particle arrangement for particle interactions in low concentrated suspension. Simulations are performed suspension with (a) two particles and (b) five particles. The marker in gray and white represents $BaTiO_3$ and Al_2O_3 respectively. The double headed arrow denotes the direction of applied AC electric field.

3.1.1. Two particle interaction

Under the specified simulation conditions $BaTiO_3$ and Al_2O_3 exhibit p-DEP and n-DEP behavior with real (CMF) values of 0.976 and -0.783, respectively. Figure 3.2 (a) and (b) show interaction of two $BaTiO_3$ and Al_2O_3 particles, respectively, two particles from each type are present in the same domain as shown in Figure 3.2 (c). The particle positions represented by markers in pink and blue for $BaTiO_3$ and Al_2O_3, respectively. The solid black curves show the path followed by the particle centers from the initial position to the final position represented by hollow and solid markers, respectively. The electric field distribution in the domain due to the presence of particles at the initial and final positions is shown in Figure 3.2 (d) - (f) and 3.2 (g) - (i), respectively.

The presence of two particles in uniform AC field, leads to the asymmetric distribution resulting in non-zero DEP force in the direction of high electric field for $BaTiO_3$ and low field for Al_2O_3. The electric field distribution shown in Figure 3.2 (d) - (f) shows the asymmetry in field around each particle with respect to the particle center. The DEP force drives the particles to rotate following antisymmetric field with respect to y-axis reducing the orientation of the particles with the electric field. The particle trajectories in Figure 3.2 (a) - (c) indicate that, the particles are pushed away from each other initially and then get attracted towards each other. The DEP force reverts to an attractive force as the orientation changes in the clockwise direction for similar particles and counter- clockwise direction when dissimilar particles are present. Therefore, the DEP particle- particle interaction always tends to attract the particles, independent of the initial particle orientation, to form a chain that is aligned parallel to the applied electric field for similar particles and perpendicular to the field for dissimilar particles as shown in Figure 3.2 (a) – (c) and (g) – (i).

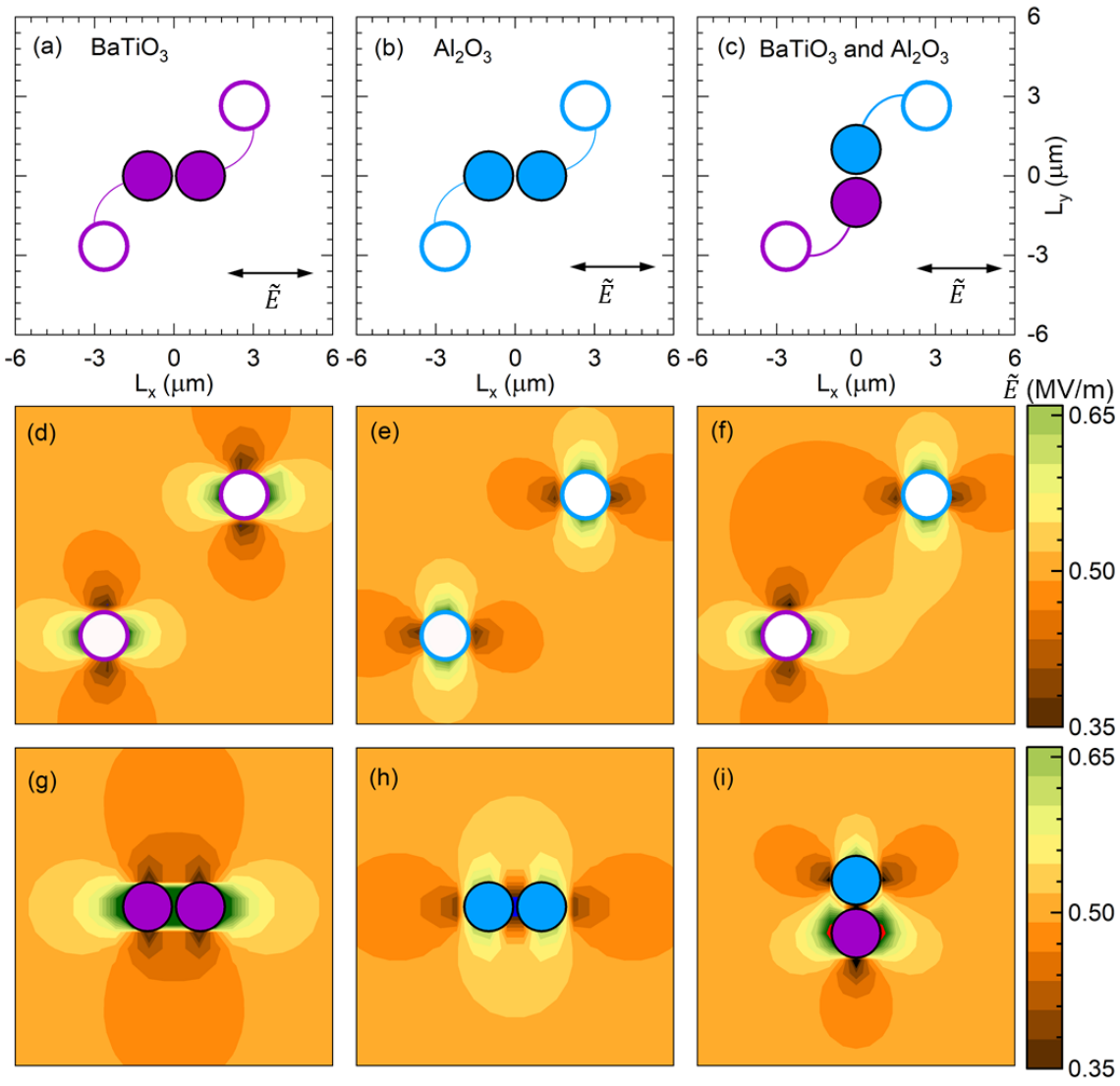

Figure 3.2. Particle arrangement in the simulation with two particles. a) $BaTiO_3$ (p-DEP) b) Al_2O_3 (n-DEP) and c) $BaTiO_3$ and Al_2O_3 (p-DEP and n-DEP, respectively). Initial and final positions are shown in hollow and solid markers, respectively. The $BaTiO_3$ and Al_2O_3 are shown in pink and blue markers, respectively and the path travelled is indicated by the solid black curve. The applied AC field direction is indicated by double headed arrow. The electric field distribution for the corresponding particle interactions in shown in the figures below in (d), (e) and (f) for the initial arrangement of particles. As the particles reach final position, the electric field gradient is reduced eventually reaching stable arrangement as shown in (g), (h) and (i).

The attractive DEP force is balanced by the repulsive hydrodynamic pressure force and particle repulsive force that increases faster than the DEP force, as the particles move closer to each other. The particle velocity decreases monotonously during the attractive motion until the electric field is symmetric around the particles as shown in Figure 3.2 (g) – (i) resulting in stable particle arrangement.

The time taken for the $BaTiO_3$ particles to form a particle pair oriented parallel to the electric field is 10.02 ms, which is 28.7% lower than the time taken for Al_2O_3 particles i.e., 14.06 ms. The difference is attributed to the p-DEP nature of $BaTiO_3$ and magnitude of real (CMF) which is 24.6% higher than Al_2O_3 particles. The perpendicular Al_2O_3 and $BaTiO_3$ particles take 11.8 ms, nearly the average amount of time taken by the individual particle pairs.

3.1.2. Five particle interaction

The particle interactions with five ceramic particles are shown in Figure 3.3. The locations of $BaTiO_3$ and Al_2O_3 particles is represented by pink and blue markers, respectively. The particle trajectories from the initial to final positions denoted by hollow and solid markers is shown by solid black curves in Figure 3.3 (a) – (c). The asymmetric electric field distribution is shown in Figure 3.3 (d) – (f) due to the initial position of particles leading to symmetric distribution shown in Figure 3.3 (g) – (i) after a particle chain is formed. Figure 3.3 (a) and (b) show the formation of particle chain parallel to the electric field involving similar $BaTiO_3$ and Al_2O_3 particles in 3.8 ms and 5.5 ms time, respectively. The particle cluster involving three Al_2O_3 particles and two $BaTiO_3$ takes 15.5 ms to form a diamond close pack arrangement as shown in Figure 3.3 (c). The longer time is required for the stable particle arrangement with $BaTiO_3$ and Al_2O_3 because the lesser force acting on Al_2O_3 particles at the far corners results in a long path followed by them.

The particle interaction with $BaTiO_3$ and Al_2O_3 particles shown in Figure 3.3 (c) indicate that the initial particle positions are responsible for the formation of a particle cluster that is not a particle chain aligned perpendicular to the direction of the field with alternating p-DEP and n-DEP particles. The patterns of particle chain can be different depending on their initial positions before the electrical field is applied, and the physicochemical properties of particles and fluids [86], but the fundamental behaviors of the particle chains or clusters remain the same.

The electric field distribution and the particle positions shown in Figure 3.3 (d) and (e) suggest slight distortion in the particles chain alignment with the direction of the field, with the distortion being greater in $BaTiO_3$. Figure 3.3 (f) shows the strong field gradient between the Al_2O_3 particle in the center of the domain and the neighboring $BaTiO_3$ particles. The DEP force on the Al_2O_3 particles placed in the far corners is weaker, as represented by the weaker field gradient around them. The $BaTiO_3$ (p-DEP) and Al_2O_3 (n-DEP) particles form a particle chain slightly sloped with the electric field which has also been observed in the experiments [87]. Therefore, the chains of multiple particles are not always aligned perfectly parallel or perpendicular to the electric field due to the influence of the surrounding particles.

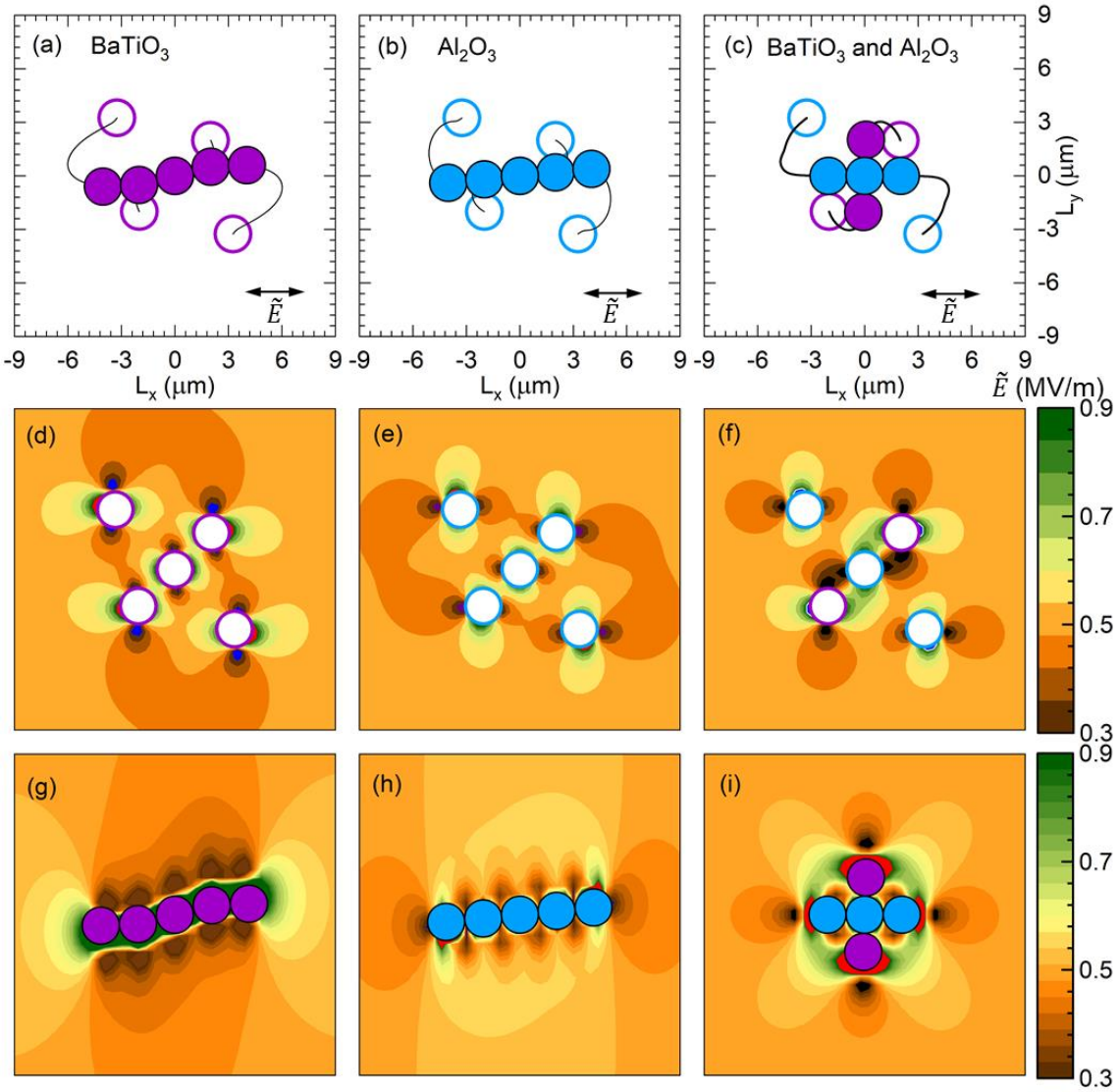

Figure 3.3. Particle arrangement in the simulation with five particles. a) $BaTiO_3$ (p-DEP) b) Al_2O_3 (n-DEP) and c) two $BaTiO_3$ and three Al_2O_3 (p-DEP and n-DEP, respectively). Initial and final positions are shown in hollow and solid markers, respectively. The $BaTiO_3$ and Al_2O_3 are shown in pink and blue markers, respectively and the path travelled is indicated by the solid black curve. The applied AC field direction is indicated by double headed arrow. The electric field distribution for the corresponding particle interactions in shown in the figures below in (d), (e) and (f) for the initial arrangement of particles. As the particles reach final position, the electric field gradient is reduced eventually reaching stable arrangement as shown in (g), (h) and (i).

3.2. PARTICLE INTERACTION IN CONCENTRATED SUSPENSIONS- SINGLE MATERIAL

20 vol. % aqueous ceramic particle suspensions involving 1024 particles suspended in two-dimensional domain are employed in the simulations. The conditions for each of the nine simulations are given in Table 1. The particle interactions are first observed in ceramic suspension with Al_2O_3 particles under low frequency (1 kHz) of applied electric field. The next set of simulations involves particle interactions at high frequency (1 MHz). The influence of initial particle arrangement through configuration A and B are studied in suspension with same type of particles ($BaTiO_3$ and Al_2O_3) and mixture of them in equal proportion. Finally, the simulations with p-DEP and n-DEP rich mixed type particle suspensions placed in configuration B are conducted.

3.2.1. Low frequency particle interaction- S1

The interaction of Al_2O_3 particles in simulation S1, initially distributed in configuration A, under 0.5 MV/m AC field at 1 kHz frequency is shown in Figure 3.4. The applied AC electric field on the initial particle distribution gives rise to dielectrophoretic force between the particles attracting them towards each other and form chains parallel to the applied electric field as the simulation progresses. The particle positions from the initial configuration leading to a stable arrangement are illustrated along with the corresponding time are shown from Figure 3.4 (a) - (d).

In the beginning of the simulation, the particles move along the y axis to compensate for the 2 μm offset between the columns of particles owing to the initial particle arrangement in configuration A, as shown in Figure 2.3 (b). During the initial vertical translational movement, the DEP force becomes attractive as the nearest particles align parallel to the field. The particles pair up with their immediate neighbors due to the attractive force while some particles near the

electrodes are pushed away from the pairs as shown in Figure 3.4 (a) at t = 15 ms. The particle pairing occurs at the corners of the domain first due to the local asymmetry in the field and continues towards the center of the domain. The particle pairs combine to grow into chains and subsequently particle clusters. Figure 3.4 (b) - (d), indicate that the chain growth occurs laterally and diagonally, with the growth of the particle chains taking priority over the alignment of the particle chains with the electric field. The particle chains near the boundary walls grow laterally, but the chains in the interior of the domain grow diagonally.

When shorter chains join with other chains present above or below them, depending on the space available for chain growth in the direction parallel to the field, the particles can form other stable arrangements besides chains, as shown in Figure 2.8. The particles in S1 organize into two types of stable arrangements as observed in Figure 3.4 (c) at t = 245 ms and (d) at t = 328 ms. The high solids loading of the suspension, spherical shape and homogeneous size facilitates the formation of these stable arrangement beyond particle chains. The diamond close pack arrangement is highlighted in red circles whereas and the partial hexagonal close pack arrangement formed when the particle chains extend in vertical direction is highlighted in blue rectangles shown in Figure 3.4 (c) and (d). By the end of the simulation, the particle chains near the electrodes are attracted towards walls and alternating regions of dense and sparse regions are formed by extending clusters creating a graded structure.

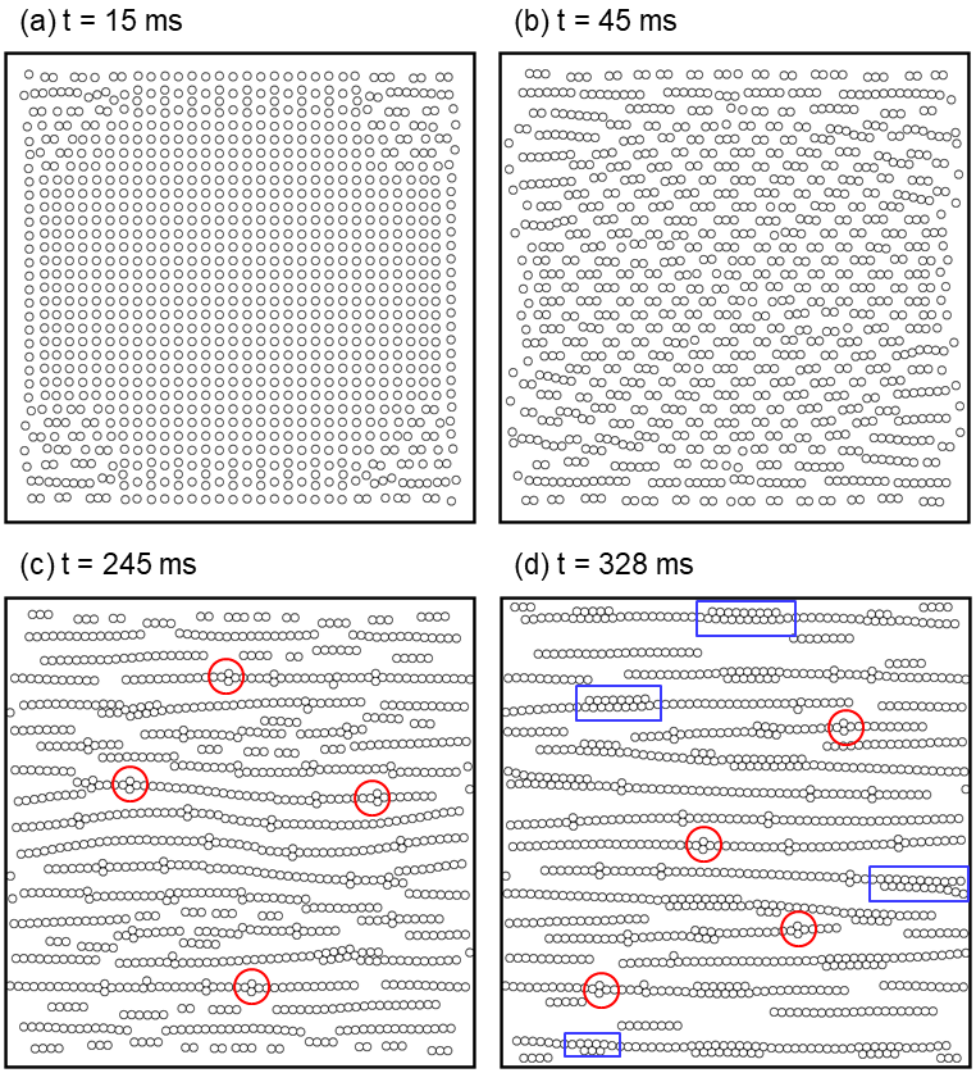

Figure 3.4. Al_2O_3 particle positions at different times in the S1 simulation

From Figure 3.4, it can also be observed that, at any instant the top and bottom halves of the particle arrangement in the domain are the mirror images of each other. The identical particle size, pattern of initial particle distribution, rectangular shape of the 2D domain and the direction of the applied electric field appear to be responsible for the symmetry in the domain.

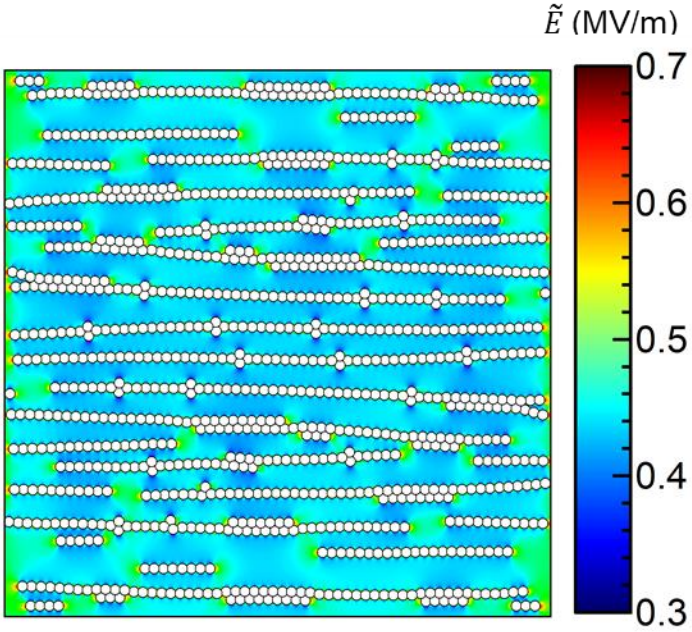

Figure 3.5. Electric field distribution in the 2D domain at the end of S1 simulation

Figure 3.5 depicts the electric field distribution in the domain at the end of the simulation for S1 after 328 ms. The smaller field gradient observed overall domain can be attributed to the low frequency condition of applied AC electric field. The p-DEP particle clusters have low electric field at top and bottom and high field along the direction of the field show that the horizontal direction is preferrable for the growth of particle chains. The electric field distribution in Figure 3.5 indicates that the parallel chains continue to follow the direction of high field to form alternating columns of particles starting at the boundary walls.

To provide a deeper insight into the particle interactions the quantitative analysis of the particle clusters formed from the start to the end of the simulation for S1 is shown in Figure 3.6. In Figure 3.6 (a) and (b) the growth of the largest cluster and the decrease in the number of independent particles that are not part of a particle chain, respectively with simulation time from 0 to 328 ms. The clusters according to Figure 3.6 (a), grow as big as 72 particles by the end of

simulation S1. The independent particles decrease in number by pairing with the particles in the center and stray particles pushed towards the electrodes joining particle chains by 91 ms as shown in Figure 3.6 (b).

The number of particle pairs is shown by solid black line in Figure 3.6 (c), indicates that the individual particles begin pairing up at 12 ms, after the initial vertical movement of particles which is perpendicular to the direction of the field, reaching a maximum of 238 pairs by 60 ms. The particle pairs continue to grow into small and medium size clusters of 3-6 particles and 7-12 particles shown in Figure 3.6 (c) and (d) by dashed and solid lines respectively, starting at 15 ms. The variation of particle clusters consisting greater than 12 particles classified as large clusters is shown in Figure 3.6 (d) represented by dashed black line presents the decrease in the number of large clusters decrease from a maximum of 30 at 120 ms to 18 by 180 ms by merging with each other and other smaller clusters. The particle cluster growth occurs rapidly till 180 ms as indicated in Figure 3.6 (c) and (d) after which the particle alignment with the direction of electric field and merging of few smaller and medium clusters with large clusters occur.

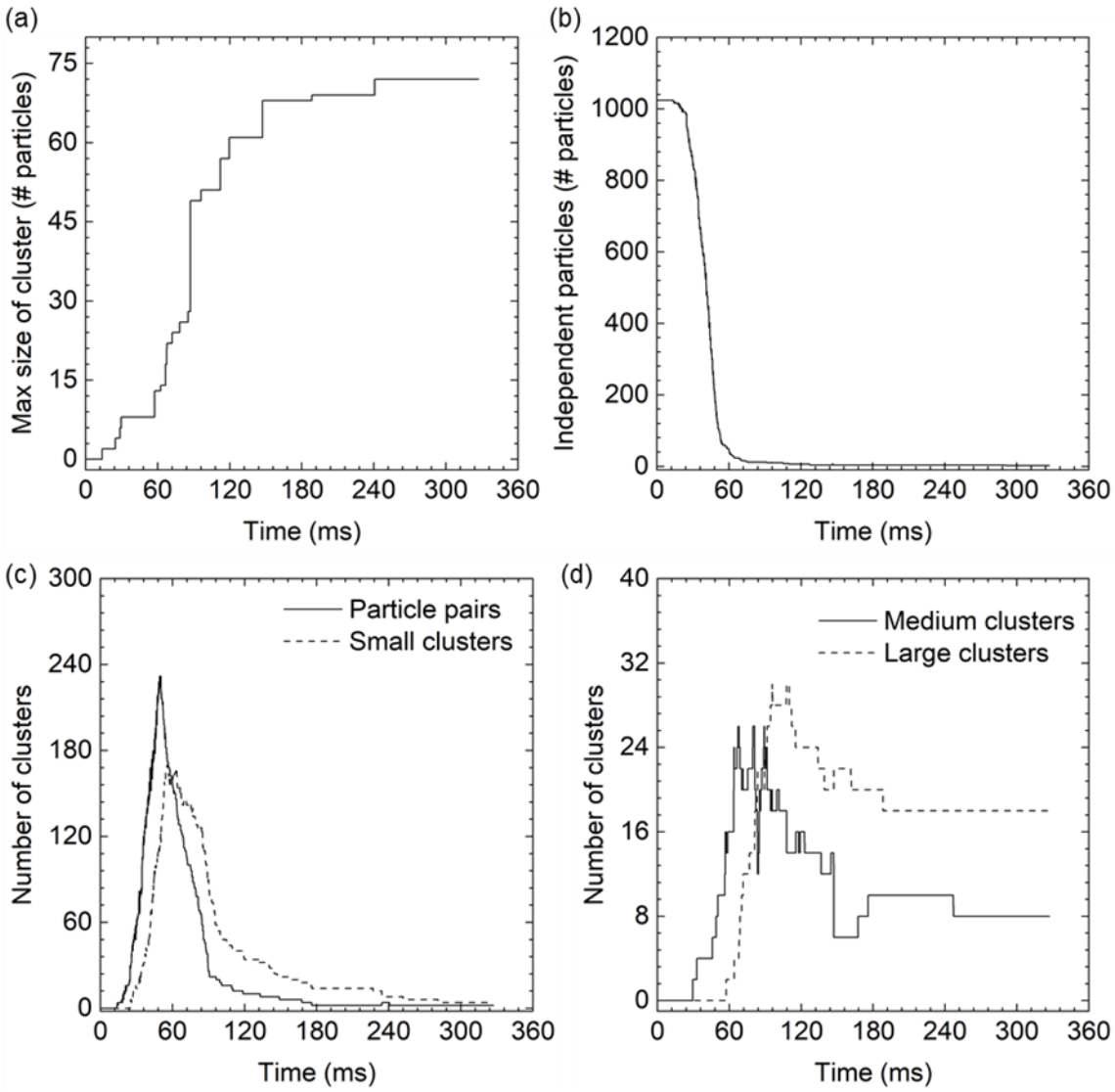

Figure 3.6. The quantitative analysis of Al_2O_3 particle cluster formation in S1. The variation of (a) size of the largest particle cluster, (b) independent particles, (c) particle pairs and small clusters (3-6 particles) and (d) medium (7-12 particles) and large (>12 particles) clusters with the simulation time is shown.

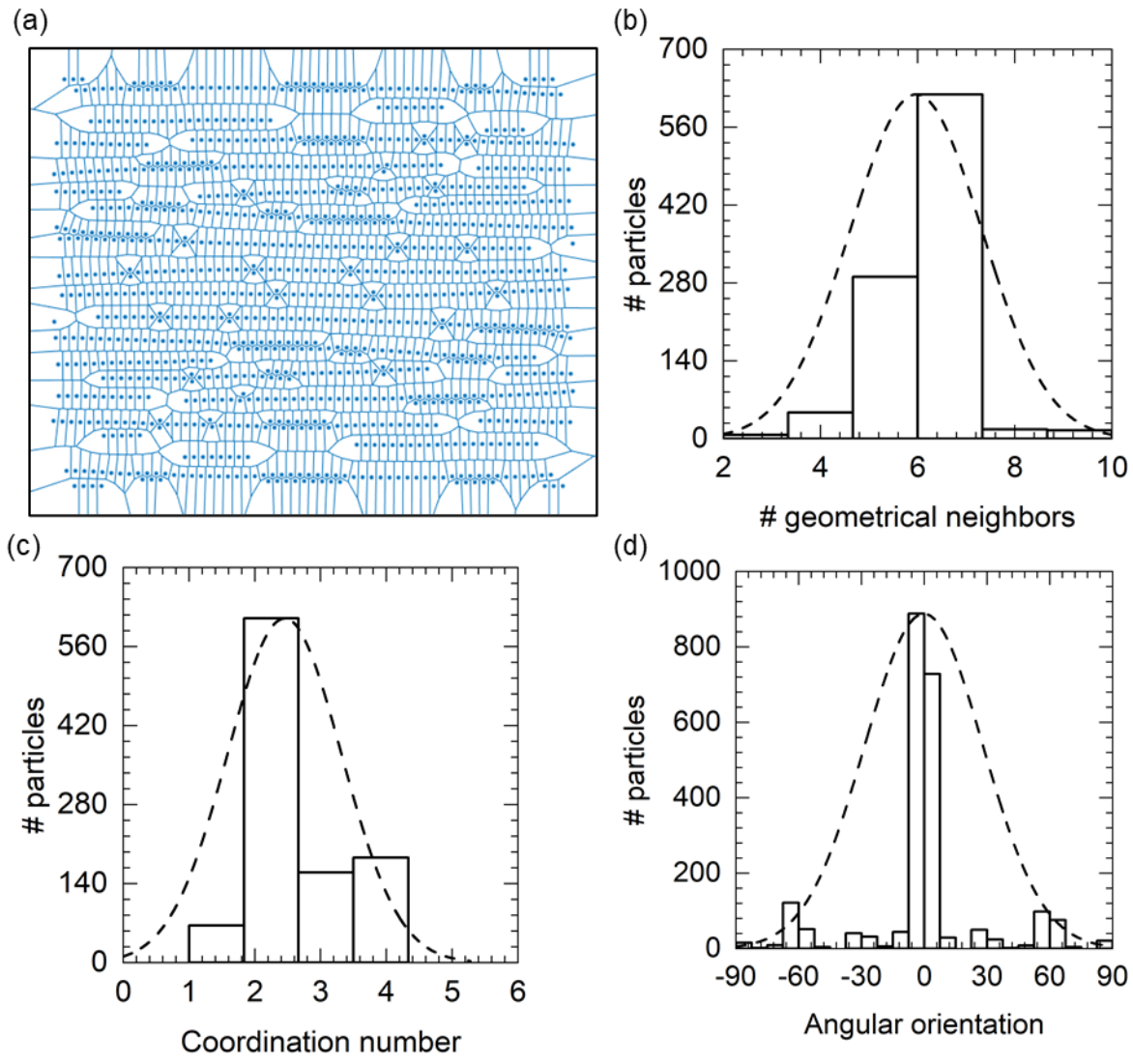

Figure 3.7. Particle packing analysis of S1. (a) Voronoi diagram to estimate the geometrical neighbors of Al_2O_3 particles at the end of S1 simulation. Distribution of (b) number of geometrical neighbors and (c) structural neighbors or coordination numbers. (d) Distribution of angular orientation of the structural neighbor pairs with the direction of applied electrical field.

The Voronoi diagram is used to estimate the geometrical neighbors of each particle in the 2D domain at the end of simulation S1 as shown in Figure 3.7 (a). The average of number of

geometrical neighbors is 5.966. The distribution of the number of geometrical neighbors shown in 3.7 (b) suggests the most particles have 6 geometrical neighbors indicating a less dense packing as the particle chains are isolated. The number of structural neighbors or the coordination number (CN) of each particle is estimated by calculating the number of particles in contact with each other with a tolerance of 0.3 μm and the distribution is shown in Figure 3.7 (c). CN_{avg} value of 2.45 and the distribution of CN indicates mostly the presence of particle chains as the maximum number of particles have 2 structural neighbors. The maximum coordination number for S1 is 4, showing the presence of particles in partial hexagonal close pack arrangement. The distribution of structural neighbors with the direction of the applied field is shown in Figure 3.7 (d). The distribution suggests that the almost all of the structural neighbors are aligned at 0° suggesting the chains are parallel and secondary peaks near ±60° are due to some particles being organized in partial hexagonal close pack arrangement.

At low AC field frequency, there is a risk of charging the electrical double layer (EDL) at the interface of particle and fluid medium. This causes bubble generation due to excessive Joule heating of the liquid and deterioration of particles [89, 88]. Therefore. AC field dielectrophoresis is preferred to be employed at high frequencies.

3.2.2. High frequency particle interaction- S2 – S5

The particle positions for Al_2O_3 and $BaTiO_3$ particles at an applied AC field frequency of 1 MHz for simulations S2, S3 and S4, S5 are shown in Figure 3.8 and 3.9, respectively. The particle positions of simulations S2 and S3 along with the corresponding simulation time for Al_2O_3 particles initially in configuration A and B are shown in Figure 3.8 (a) – (c) and (d) – (f), respectively. The $BaTiO_3$ particle positions and corresponding time in simulations S4 and S5, initially in configuration A and B are shown in Figure 3.9 (a) – (c) and (d) – (f). The quantitative

analysis of the particle clusters for simulations with Al_2O_3 and $BaTiO_3$ are shown in Figure 3.10 and 3.11, respectively, where the particles with interparticle distance less than 0.4 μm are considered to belong to a cluster.

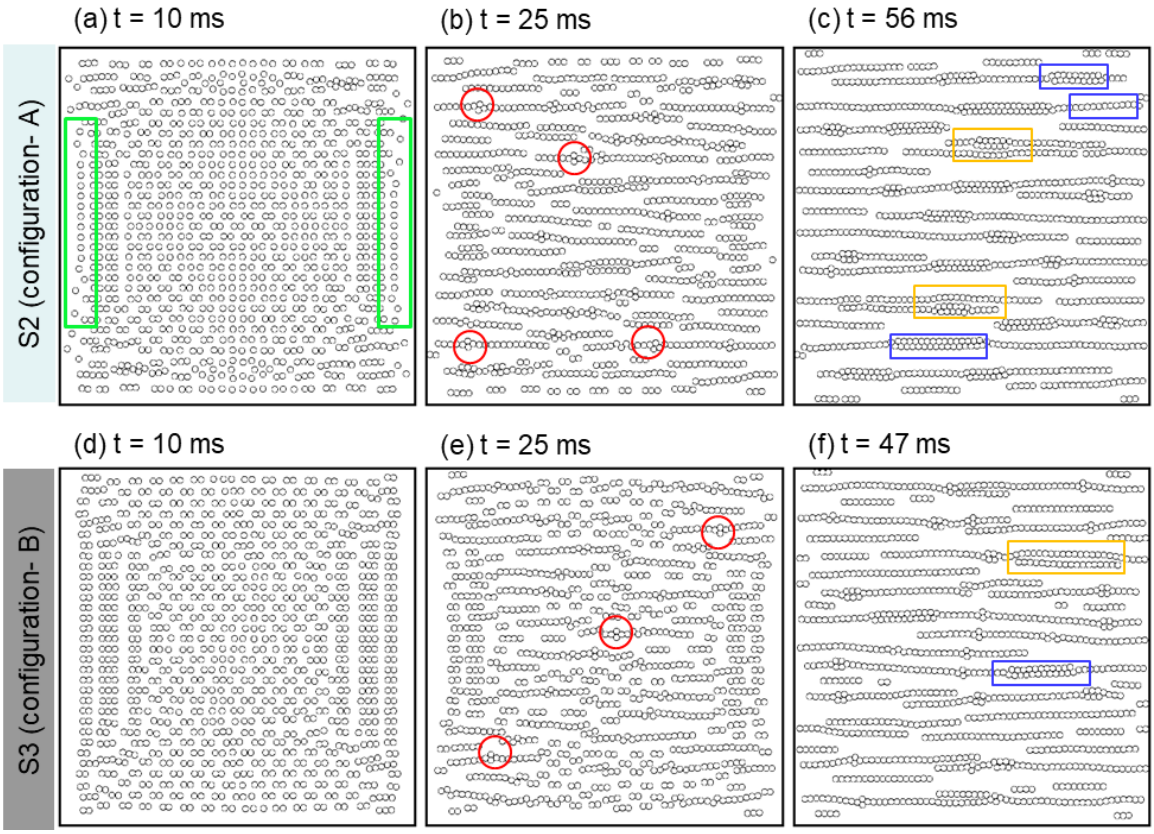

Figure 3.8. Al_2O_3 particle positions at different times in (a) – (c) S2 simulation and (d) – (f) S3 simulation

The particle cluster formation begins and propagates in S2 - S5 similar to S1 as they fundamentally employ single type of ceramic particles uniformly distributed in aqueous suspension. This is supported by the decrease in the independent particles is shown in Figure 3.10 (b) and 3.11 (b), and the corresponding growth of the largest cluster presented in Figure 3.10 (a)

and 3.11. (a), for Al_2O_3 and $BaTiO_3$, respectively. The variation in simulations due to the difference in particles configuration A and B is represented by solid black and dashed blue lines, respectively.

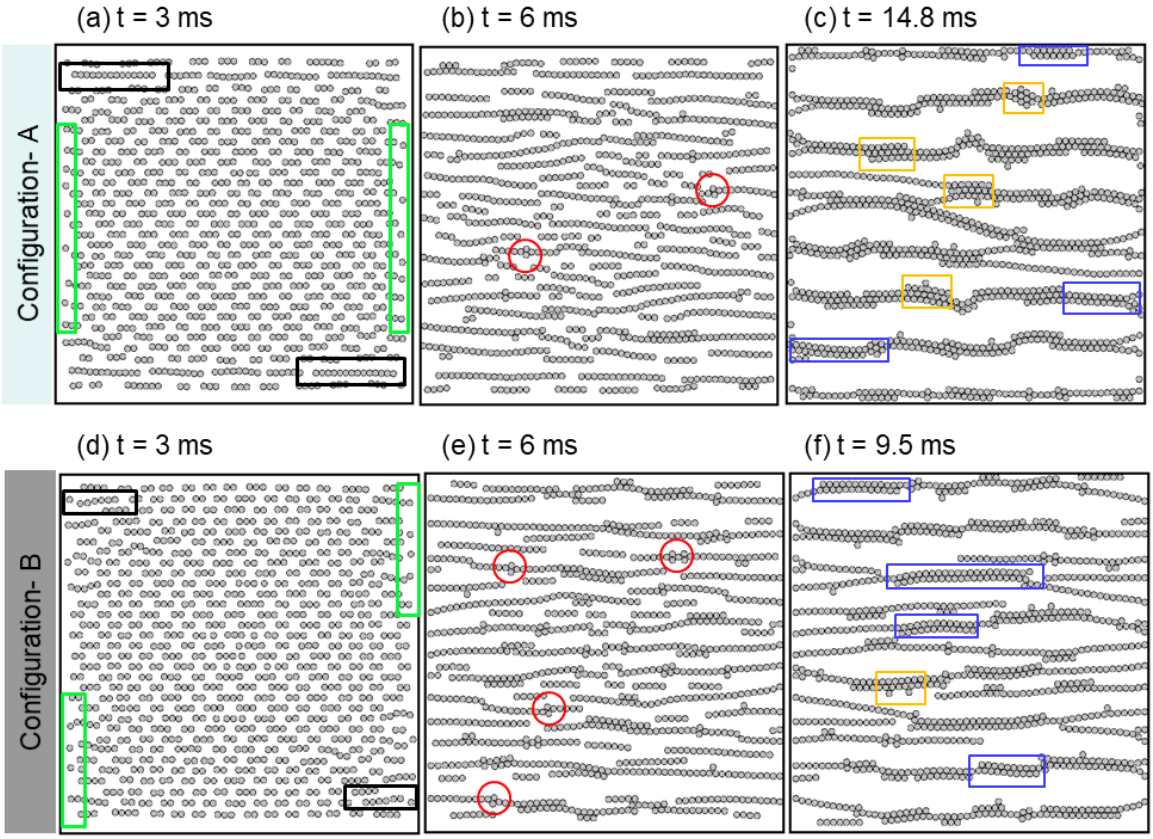

Figure 3.9. $BaTiO_3$ particle positions at different times in (a) – (c) S4 simulation and (d) – (f) S5 simulation

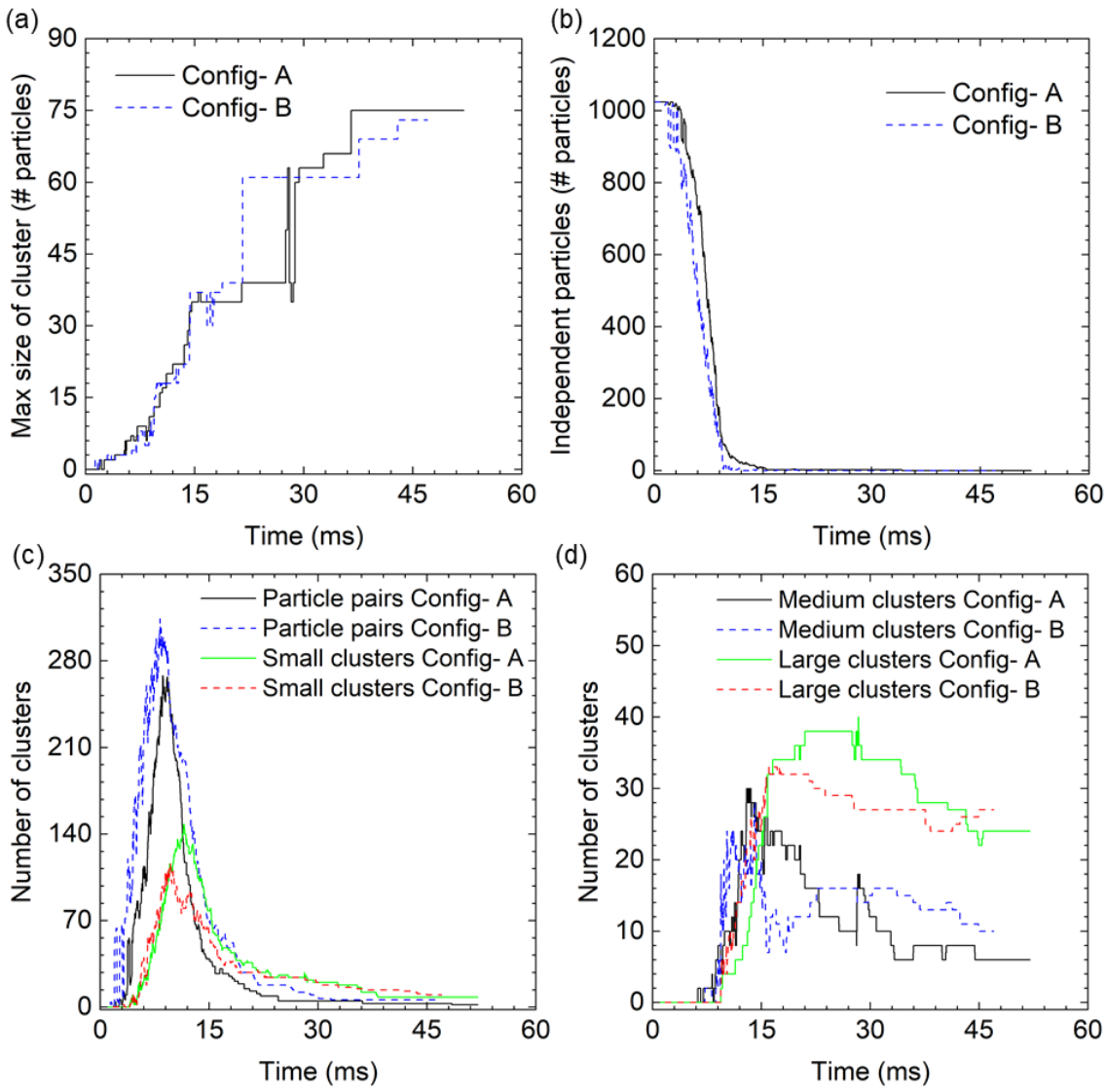

Figure 3.10. The quantitative analysis of Al_2O_3 particle cluster formation in S2 (configuration A) and S3 (configuration B). The variation of (a) size of the largest particle cluster (b) independent particles, (c) particle pairs and small clusters (3-6 particles) and (d) medium (7-12 particles) and large (>12 particles) clusters with the simulation time is shown.

The particles in simulations with single type of material begin to form pairs beginning at the corners of the 2D domain and continue towards the interior of the domain. Due to higher average interparticle distance in configuration A of 4.01 μm compared to 3.71 μm in configuration

B, particle chaining begins in S3 and S5 earlier than S2 and S4. Figure 3.8 (a) and (d) at t = 10 ms show that the initial particle pairing leaves out some unpaired particles near the electrodes in S2 highlighted in green rectangles are absent in S3 simulation for Al_2O_3. The independent particles reach their minimum value in 15 ms for S2 whereas it takes only 9 ms for particles in S3 as shown in Figure 3.10 (b), proves that the closer proximity saves the simulation time due to larger DEP force acting on particles.

The difference in the initial interparticle distances between the two configurations does not affect the process of some unpaired particles being pushed towards the electrodes for $BaTiO_3$. As pairing occurs more rapidly than the vertical particle movement perpendicular to the direction of the field in the beginning of the simulations S4 and S5 unpaired particles are present in the domain as evident by the particles highlighted in green rectangles shown in Figure 3.9 (a) and (d) at t= 3 ms. However, the length of the long particle chains highlighted in blue ovals located near the four corners of the 2D domain highlighted by black rectangles in Figure 3.9 (a) and (d) show that the pace of particle chain growth occurs much faster in S5 than in S4.

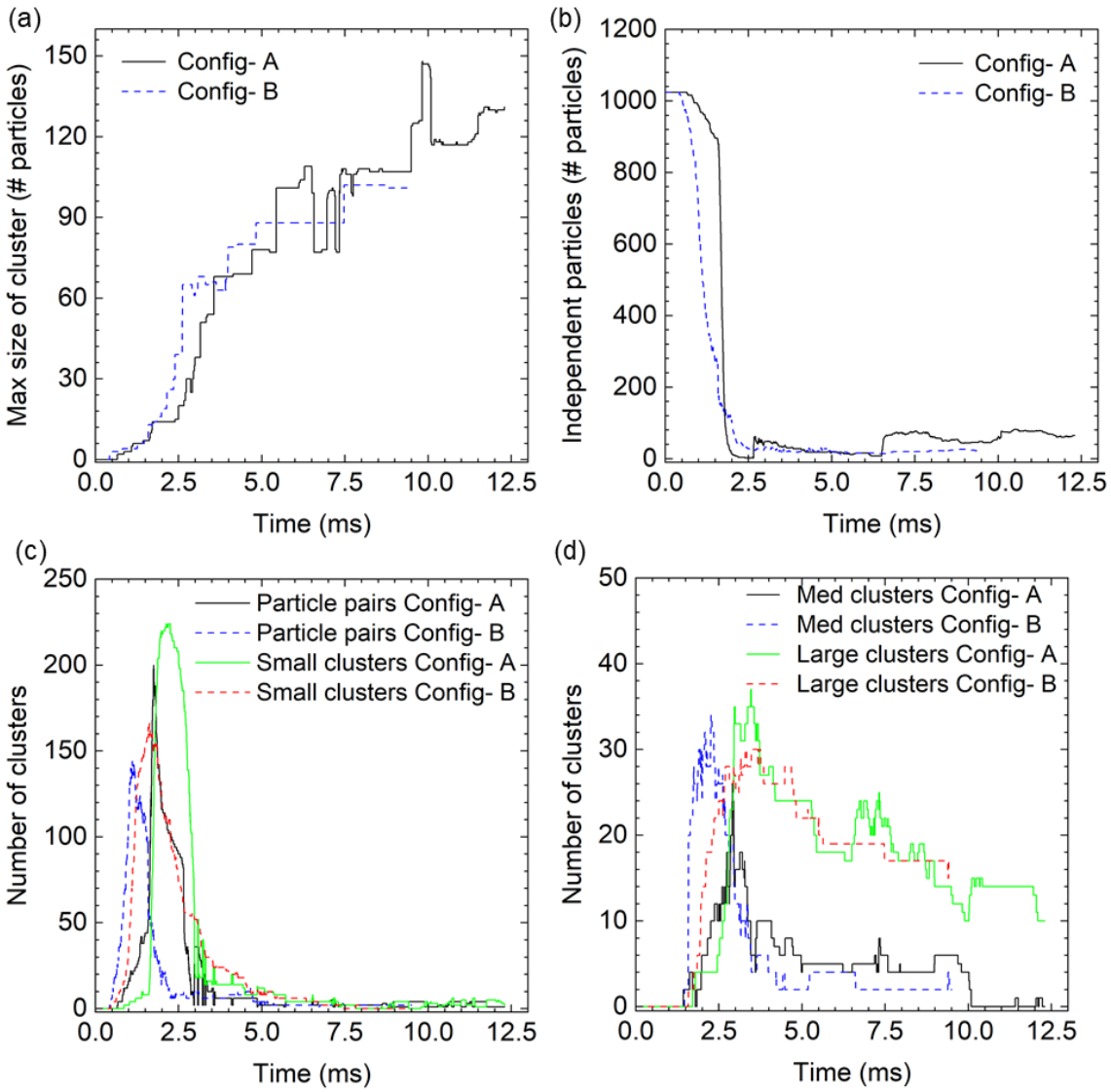

Figure 3.11. The quantitative analysis of $BaTiO_3$ particle cluster formation in S4 (configuration A) and S5 (configuration B). The variation of (a) size of the largest particle cluster (b) independent particles, (c) particle pairs and small clusters (3-6 particles) and (d) medium (7-12 particles) and large (>12 particles) clusters with the simulation time is shown.

The formation and growth in number of particle pairs with the simulation time in S2 and S4 are denoted by solid black lines and in S3 and S5 by dashed blue lines in Figure 3.10 (c) and 3.11 (c). The variation in the number of small clusters (3-6 particles) in S2 and S4 are denoted by

solid green lines and in S3 and S5 by dashed red lines in Figure 3.10 (c) and 3.11 (c). The particle pairing is slightly delayed due to longer path in configuration A, beginning at 2.1 ms for S2 with a maximum of 252 pairs by 11.8 ms compared to the pairing starting at 1.8 ms for S3 with a maximum of 296 pairs by 10.5 ms. The higher number small clusters that grow from the particle pairs in S3 than S2 with 141 and 103 clusters, respectively is also as an account of the neighbors being closer in configuration B.

Although the average interparticle distance is smaller in configuration B prompting particle pairing and subsequent formation of small clusters to occur quickly in S5 than in S4, as shown in Figure 3.10 (c). The number of pairs and small clusters are fewer in S5 reaching a maximum 204 pairs at 1.8 ms compared to 142 pairs at 0.9 ms for S4. The maximum number of small clusters in S4 is 236 are formed at 2.5 ms, and in S5 are 181 are formed at 0.9 ms and 1.6 ms respectively. There are fewer small particle clusters and pairs in S5 because the particles quickly join to form medium and large sized clusters because the neighbors are closer than in S4.

The independent particles and pairs combine and grow to form longer chains and particle clusters as shown in Figure 3.8 (b) and (e) at t = 25 ms for simulations S2 and S3 for Al_2O_3 and Figure 3.9 (b) and (e) at t = 6 ms for simulations S4 and S5 for $BaTiO_3$ particles, respectively. Figure 3.8 (c) and (f) at t = 56 ms and 47 ms, 3.9 (c) and (f) at t = 14.8 ms and 9.5 ms, indicate that the diamond close pack arrangement shown in red circles of the particles was observed to be prominent in S1, but because of the high AC field frequency in S2 - S5, they reorganize to form partial hexagonal close pack arrangement shown in blue rectangles. The particles in diamond arrangement rotate counter- clockwise to form longer chains or particle clusters with partial hexagonal close pack arrangement in S2 – S5, and hexagonal close pack arrangement in S4 and S5 shown in yellow rectangles in Figure 3.9 (c) and (f). The chain growth prominently occurs in

the direction parallel to the applied field, especially in S2 and S3 as evident from the isolated particle chains in Figure 3.8. (b), (c), (e) and (f). For p-DEP $BaTiO_3$ particles, the growth of chains is significant in the vertical direction from the long- curved chain segments in Figure 3.9 (b), (c), (e) and (f) for simulations S4 and S5. The Al_2O_3 particle clusters when merged vertically seem to be repeal the combining two segments after donating a particle as shown in yellow rectangle in Figure 3.8 (c) and (f).

The variation of number of medium clusters (7-12 particles) with the simulation time in S2 and S4 are denoted by solid black lines and in S3 and S5 by dashed blue lines. The large clusters (>12 particles) in S2 and S4 are denoted by solid green lines and in S3 and S5 by dashed red lines are shown in Figure 3.10 (d) and 3.11 (d). The number of medium sized clusters by the end of simulation in S4 and S5 with values 1 and 4 are lower than, S2 and S3 with values 11 and 7, respectively. The number of large clusters of $BaTiO_3$ are also fewer with 10 and 12 clusters in S4 and S5, than Al_2O_3 particles in S2 and S3 with 24 and 28 clusters, respectively. However, the final size of largest clusters in S4 and S5 are 96 and 122 particles and in simulations S2 and S3 are 74 and 72 particles, respectively. Therefore, only a nominal difference in the cluster size, number of clusters, final particle distribution accounting for the difference in time, between the simulations performed with particles in configuration A and B is observed. This suggests that although the initial configuration affects the rate of cluster formation, it does not have an impact on the pattern of final particle distribution as shown in Figure 3.8 (c) and (f) for S2 and S3 and in Figure 3.9 (c) and (f) for S4 and S5.

As the absolute value of the real (CMF) of the particle increases the time required for the formation of stable particle arrangement in the form of chains and clusters decreases. In S4 and S5 simulations, respectively, large clusters with stable arrangements are formed by 10 ms, whereas

the simulations S2 and S3 took nearly 4 times i.e., 40 ms. This difference is greater than what was observed in preliminary observations involving two and five particles, showing that the factors affecting the chain formation exist beyond the magnitude of real (CMF). The difference in time taken, also supports the findings of Xie et al. [90]. that the time taken for the pearl chain formation of p-DEP particles is lower than n-DEP particles

The applied frequency, type of DEP effect and the magnitude of real (CMF) affect the size of the clusters and the corresponding time taken for the cluster formation. In the simulations where AC electric field is applied at high frequency (1 MHz), the spatial non-uniformity of the electric field around particles is higher causing them to vibrate. As the particles join together to form chains the oscillation of particles is reduced and become more stable as they form longer chains.

The higher amplitude of particle vibration causes the chains to align at high angle with the electric field to form larger particle clusters. Therefore, the particle clusters in S4 and S5 shown in Figure 3.9 (c) and (f), contain long curved segments and are denser than S2 and S3 shown in Figure 3.8 (c) and (f). The amplitude of particle vibrations is exacerbated in $BaTiO_3$ separating it from the cluster and affecting the size which increases with the magnitude of the variable time step used to estimate the subsequent position of the particle. Therefore, in Figure 3.11 (a) and (b) jagged curves are observed, and the number of independent particles is higher in S4 due to greater time step than in S5 as shown in Figure 3.11 (b) with 36 and 15 particles, respectively.

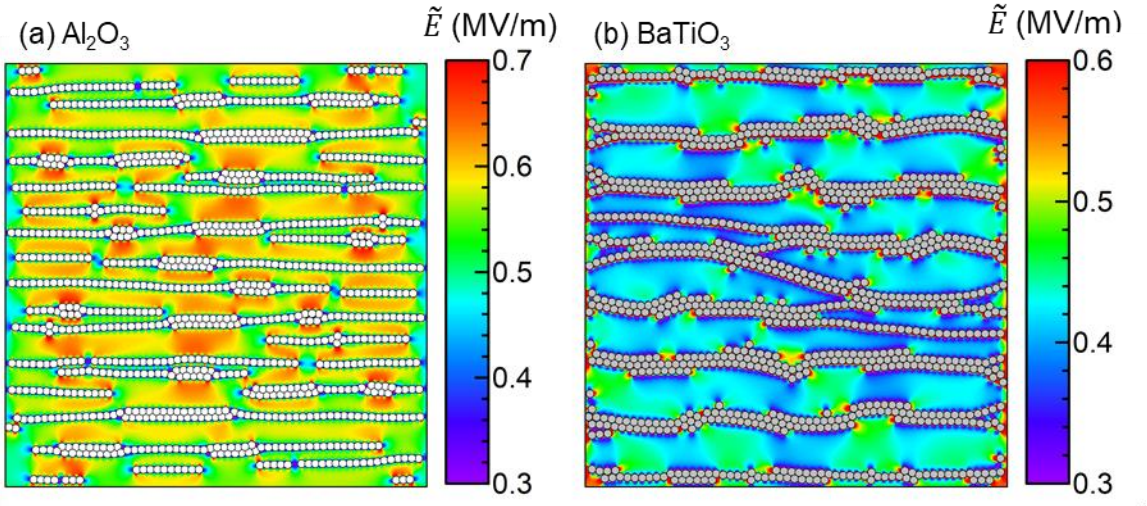

Figure 3.12. Electric field distribution in the 2D domain at the end of (a) S2 and (b) S4 simulations

Figure 3.12 (a) and (b) show the electric field distribution in the 2D domain for the particle arrangement at the end of simulations S2 and S4. The high field strength regions between chains are observed between the particle clusters in Figure 3.12 (a) due to n-DEP type Al_2O_3 particles and low field regions in Figure 3.12 (b) $BaTiO_3$ particle clusters from p-DEP effect. However, the paths of attractive DEP force due to field gradient existing between the particle clusters indicate that the clusters in close proximity will eventually coalesce to form hexagonal close pack arrangement, it occurs much more rapidly in S4 than in S2. These paths also show how the particle clusters curve and reach out to the neighboring clusters above or below them.

Figure 3.13 and 3.14, show the analysis of the final particle distribution in the 2D domain for S2 and S4. The number of geometrical neighbors of each particle in the domain is estimated using the Voronoi diagrams as shown in Figure 3.13 (a) and (b) for S2 and S4, respectively. The average number of geometrical neighbors for S2 is 5.959, which is slightly higher than for S4 which is 5.957. The difference in distribution of number of geometrical neighbors in S2 and S4

shown in Figure 3.14 (a) reveals larger number of particles with higher geometrical neighbors. This difference is indicative of less dense packing of Al_2O_3 particles with separated clusters in S2 than interconnected $BaTiO_3$ clusters in 2D domain in S4. The particles at the boundaries of chains or clusters and isolated particle chains have higher number of geometrical neighbors, hence despite the dense packing and interconnectivity between clusters in S4, the difference in the value of average geometrical neighbors between S2 and S4 is very low.

The number of structural neighbors whose interparticle distance is less than 0.4 um is used to estimate the coordination number (CN). The distribution of CN of particles in S2 and S4 is presented in Figure 3.14 (b), showing particles in S4 have higher CN. The value of CN_{avg} for S4 is 2.84, which is much higher than Al_2O_3 particles in S2 with a value of 2.33. The maximum value of CN observed in S2 is 4 and S4 is 6 due to partial hexagonal close pack and hexagonal close pack arrangement, respectively. The distribution of CN for Al_2O_3 particles in S2 and S1 as seen in Figure 3.14 (b) and 3.7 (c) signify close similarity of the final particle distributions.

The orientation of structural neighbor pairs with the direction applied field is calculated and the distribution is shown in Figure 3.14 (c) for S2 and S4. The angular distribution suggests that the particles in S2 are distributed primarily in the form of chains aligned parallel to the field whereas, the particles in S4 are present in hexagonal close pack arrangement due to the peaks at ±60°.

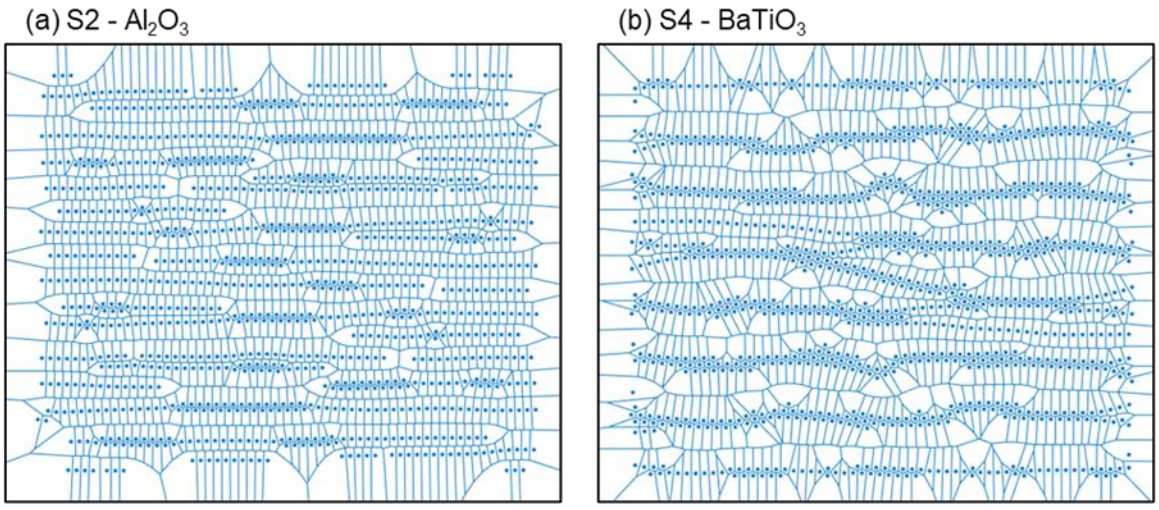

Figure 3.13. Voronoi diagram to estimate the number of geometrical neighbors for the particle distribution at the end of simulation (a) S2 (Al_2O_3) and (b) S4 ($BaTiO_3$).

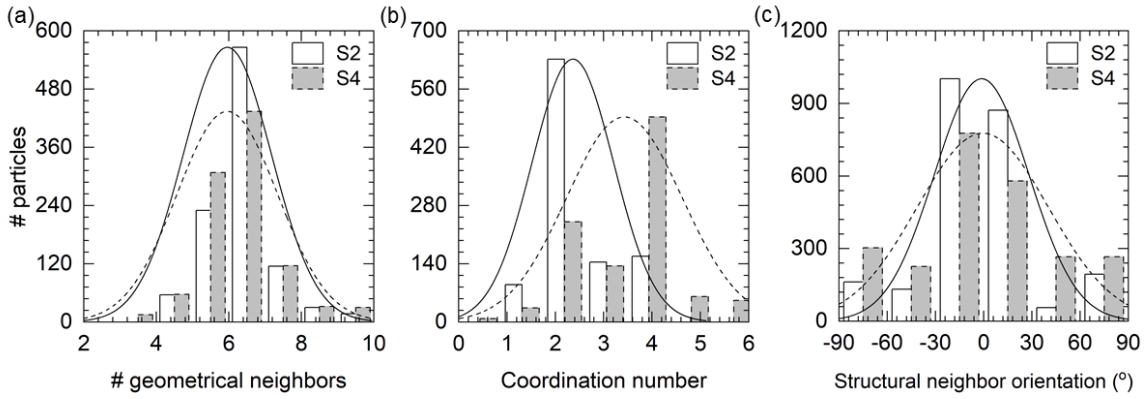

Figure 3.14. Particle packing analysis at the end of simulations S2 and S4. The distribution of (a) number of geometrical neighbors (b) structural neighbors or coordination number and (c) structural neighbor orientation with the direction of the field.

3.3. PARTICLE INTERACTION IN CONCENTRATED SUSPENSIONS- MIXED MATERIAL

The particle interactive motion when two particle types are involved is investigated by placing Al_2O_3 and $BaTiO_3$ particles in the same domain. From Table 2.2, M1 and M2 simulations, 512 particles of Al_2O_3 and 512 particles of $BaTiO_3$ are arranged in configuration A and B, respectively. For the simulations N1 and N2, Al_2O_3 and $BaTiO_3$ in the composition of 820:240 particles and 204:820 particles, respectively are arranged in configuration B.

3.3.1 Suspensions with equal proportion of Al_2O_3 and $BaTiO_3$- M1 and M2

Al_2O_3 and $BaTiO_3$ particles acquire n-DEP and p-DEP properties under the simulation conditions for M1 and M2. The dissimilar type of particles located in the electric field, leads to pearl chains aligned perpendicular to the applied electric field are created. Figure 3.15 and 3.16 show the particle positions from the beginning of the simulation to the end of the simulation for M1 and M2, respectively. The arrangement of particles in M1 and M2 is according to configuration A and B, respectively as shown in Figure 3.15 (a) and 3.16 (a) at t = 0.

At the outset of the simulation, Al_2O_3 and $BaTiO_3$ particles form pairs aligned perpendicular to the field direction as shown in Figure 3.15 (b) and 3.16 (b) at t=3 ms. However, the subsequent particle interactions shown in Figure 3.15 (c) and 3.16 (c) at t = 14 ms suggest that the chain growth of alternate Al_2O_3 - $BaTiO_3$ particles perpendicular to the field after the initial pairing does not occur. The higher magnitude of real (CMF) of $BaTiO_3$ prompts the perpendicular Al_2O_3 - $BaTiO_3$ particle chains to break apart and prioritize the formation of long parallel $BaTiO_3$ chains as indicated by Figure 3.15 (c) and 3.16 (c).

The absence of $BaTiO_3$ clusters with thickness > 2 particles in Figure 3.15. (c) – (d) and 3.16 (c) - (d) implies that presence of Al_2O_3 hinders the formation of hexagonal close pack arrangement of $BaTiO_3$ particles. The Al_2O_3 particles however enter partial hexagonal close pack

arrangement between long $BaTiO_3$ particle chains. The Al_2O_3 clusters grow in directions both parallel and perpendicular to the field being trapped and transported by the $BaTiO_3$ particle chains. The diamond close pack arrangement of particles is not observed in the regions of randomly packed Al_2O_3 particles separated by long $BaTiO_3$ chains which indicate existence of a certain threshold of particle concentration in the suspension to achieve and maintain it. Figure 3.15 (d) and 3.16 (d) at t = 30 ms and 27 ms, respectively, suggest that the long $BaTiO_3$ chains are separated by clusters of Al_2O_3 particles which resembles a composite structure. The clusters of Al_2O_3 particles leave an empty region in the second and fourth quadrant of the 2D domain. The symmetry that was maintained in the particle distribution with single type of material is not observed in mixed particle simulations as seen in Figure 3.15 (d) and 3.16 (d).

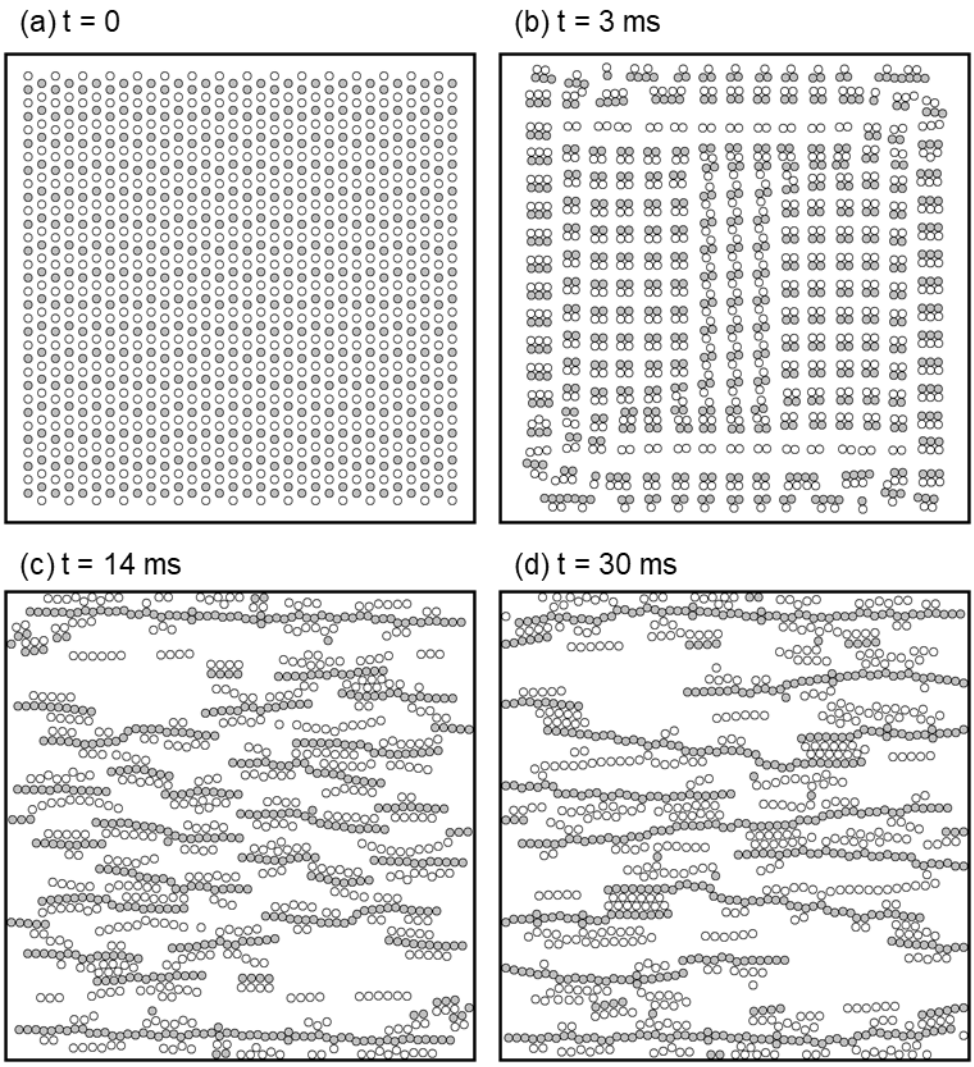

Figure 3.15. Al_2O_3 and $BaTiO_3$ particle positions indicated by white and gray markers respectively, at different times in M1 simulation

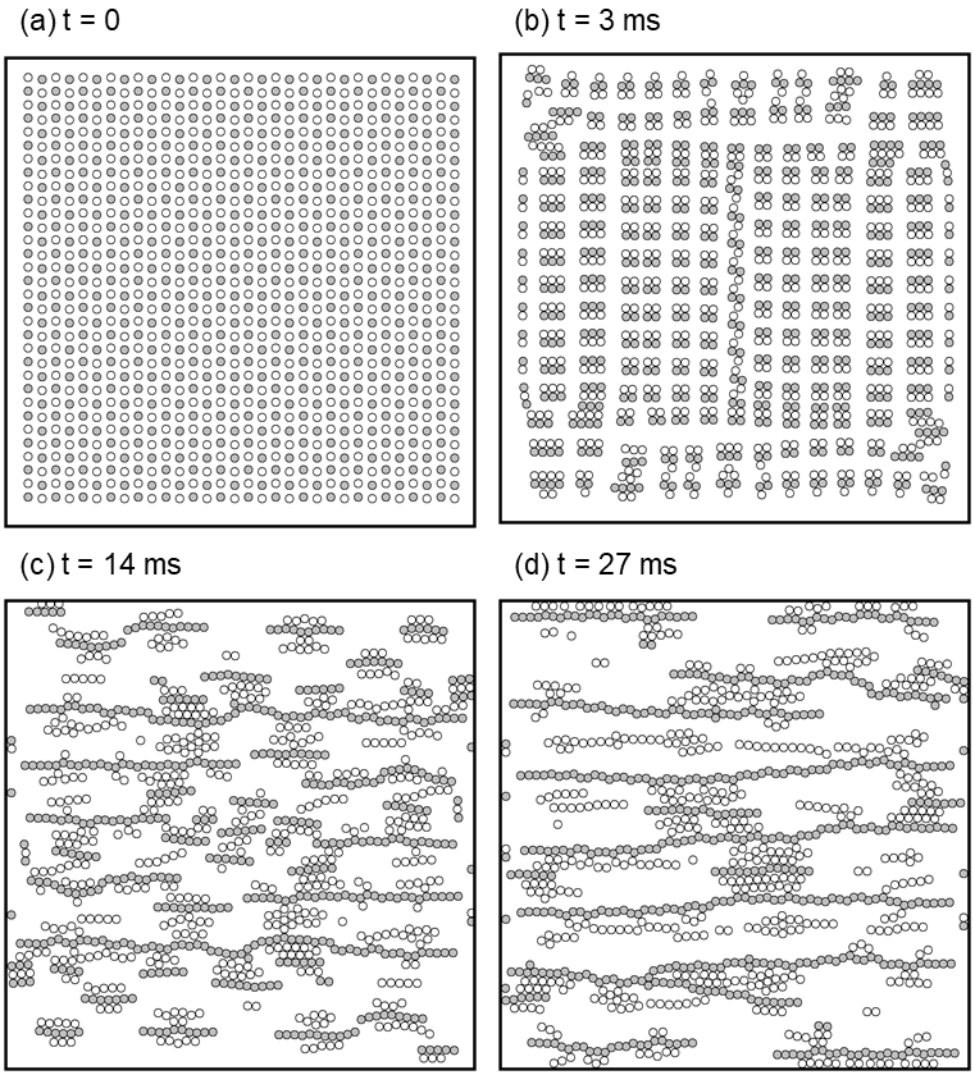

Figure 3.16. Al_2O_3 and $BaTiO_3$ particle positions indicated by white and gray markers respectively, at different times in M2 simulation

The effect of initial particle location has is discovered to be significant on final particle distribution in simulations with mixed type of particles than in S2 - S5. In M1 simulation, the proximity of the Al_2O_3 particles on the edges of the initial particle distribution is closer to the top and bottom insulated boundary walls, this allows for the particle pairs formed to move towards them and away from the center as indicated in Figure 3.15 (c). The particle distribution in

configuration A is also responsible for the formation of parallel Al_2O_3 short chains away from the $BaTiO_3$ clusters. Figure 3.16 (d) shows that the particles in contact with the top and bottom boundary walls are fewer in M2 owing to configuration B.

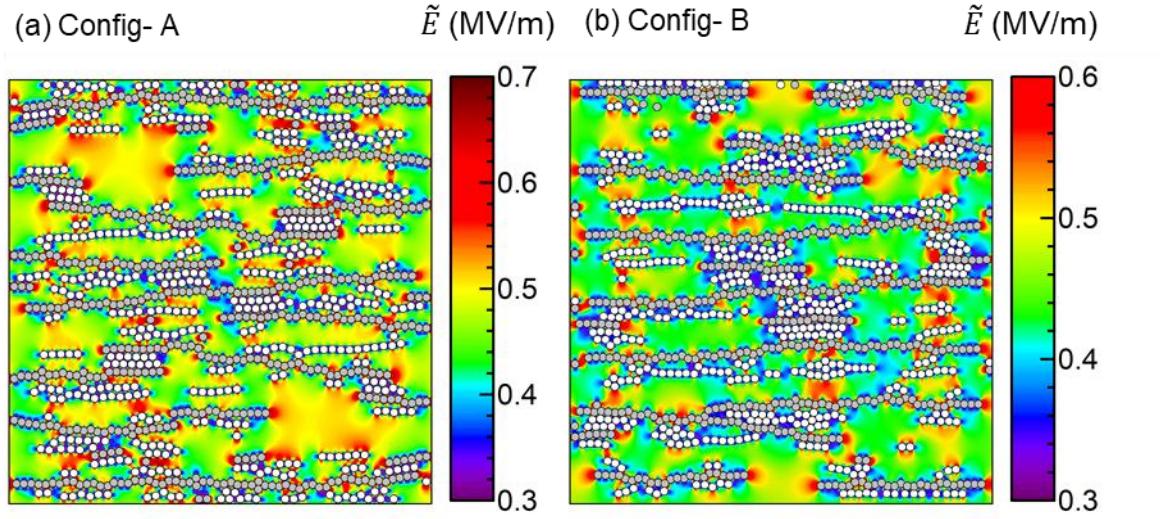

Figure 3.17. Electric field distribution in the 2D domain at the end of (a) M1 (configuration A) and (b) M2 (configuration B) simulation. The gray and white markers represent $BaTiO_3$ and Al_2O_3 particles, respectively.

The particles interact to form clusters and reach stable arrangements in M1 and M2 simulations in 30 ms and 27 ms respectively which is nearly the average of the time taken by individual particles in S2 - S5. The electric field distribution in the domain for M1 and M2 simulations is shown in Figure 3.17 (a) and (b), respectively. The domain is characterized by extensive regions of high field strength which separate the particle clusters, whereas the regions

of low field strength are occupied by Al_2O_3 particles. This indicates that the movement of $BaTiO_3$ precedes and influences the mobility of Al_2O_3.

The number of geometrical neighbors of particles in the 2D domain at the end of M1 and M2, is estimated from the Voronoi diagram shown in Figure 3.18 (a) and (b). The average number of geometrical neighbors for M1 and M2 are 5.955 and 5.967, respectively. The higher value of M2 indicating separated particle clusters, is because of the more scattered Al_2O_3 particles. The distribution of geometrical neighbors, CN and structural neighbor orientation shown in Figure 3.19 (a) - (c) for M1 and M2 suggest that the particle distributions at the end of simulation are similar. However, the higher CN_{avg} of 2.37 for M2 compared to 2.25 for M1 indicates a denser packing due to the lower interparticle distance in the initial particle distribution in configuration B. Although, the peak of distribution of structural neighbor orientation with the direction of field is at 0° suggesting the dominance of particle chains aligned with the direction of the field, secondary maxima are observed at 90° and 60°. This is due to the partial hexagonal close pack arrangement of Al_2O_3 particles and $BaTiO_3$ - Al_2O_3 pairs among the long $BaTiO_3$ chains.

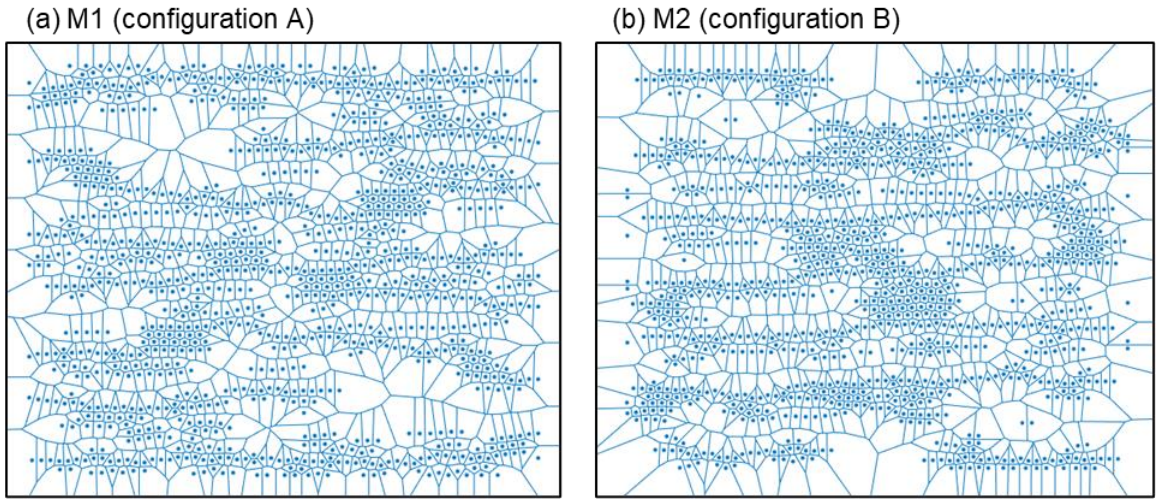

Figure 3.18. Voronoi diagram to estimate the number of geometrical neighbors for the particle distribution at the end of simulation (a) M1(configuration A) and (b) M2 (configuration B).

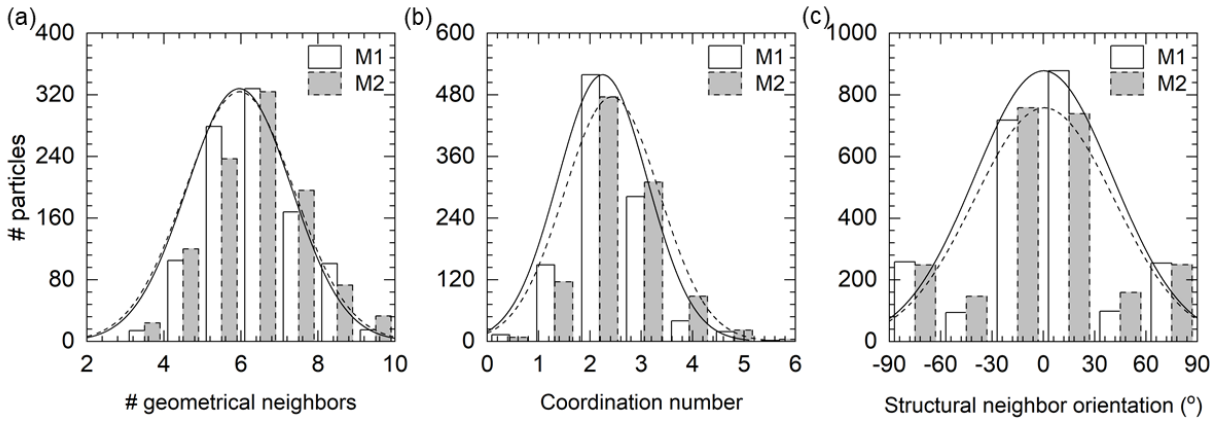

Figure 3.19. Particle packing analysis at the end of simulations M1 and M2.Distribution of (a) number of geometrical neighbors (b) structural neighbors or coordination number and (c) structural neighbor orientation with the direction of the field.

3.3.1 Mixed material simulation- N1 and N2

N1 and N2 simulations presents the particle interactions in a p-DEP and n-DEP particle dominant suspensions respectively, with 204 Al_2O_3 and 820 $BaTiO_3$ particles for N1 and 820 Al_2O_3 and 204 $BaTiO_3$ particles for N2, in configuration B. Figure 3.20 and 3.21 shows the particle positions from the beginning to the end of the simulation for N1 and N2, respectively.

The p-DEP behavior combined with high magnitude of real (CMF) of $BaTiO_3$ particles contribute to the formation of short $BaTiO_3$ chains and absence of Al_2O_3 - $BaTiO_3$ pairs at the immediate outset of the N1 as opposed to the formation of particle pairs observed in the other cases, as shown in Figure 3.20 (b) at t = 2 ms. The presence of Al_2O_3 particles scattered uniformly across the domain promotes the formation of long $BaTiO_3$ chains more rapidly than in S3. The subsequent particle interactions observed in Figure 3.20 (c) and (d) at t = 7 ms and 13 ms, respectively, suggest that the short and medium $BaTiO_3$ chains as they navigate around the Al_2O_3 particles chain to grow into long chains. Similar to simulation S4 and S5, the $BaTiO_3$ chains are attracted towards the boundary walls with alternating dense and sparse regions in the domain, but the presence of Al_2O_3 in the suspension causes $BaTiO_3$ clusters to be less thick and curved.

In N2, the Al_2O_3 particle rich composition and initial distribution allows, Al_2O_3 - $BaTiO_3$ perpendicular pairs and Al_2O_3 parallel pairs to be formed in the beginning of the simulation after which $BaTiO_3$ attracts the Al_2O_3 particle pairs creating an ‘L’ shape particle arrangement which are distributed as mirrored pairs across the domain as shown in Figure 3.21 (b) at t = 3 ms. The mirrored pairs join at the horizontal segment with Al_2O_3 particles growing laterally. Figure 3.21 (c) at t = 15 ms shows the Al_2O_3 particles settle into a diamond arrangement with the top and bottom ends attached to $BaTiO_3$ - Al_2O_3 particle pair, resembling spade.

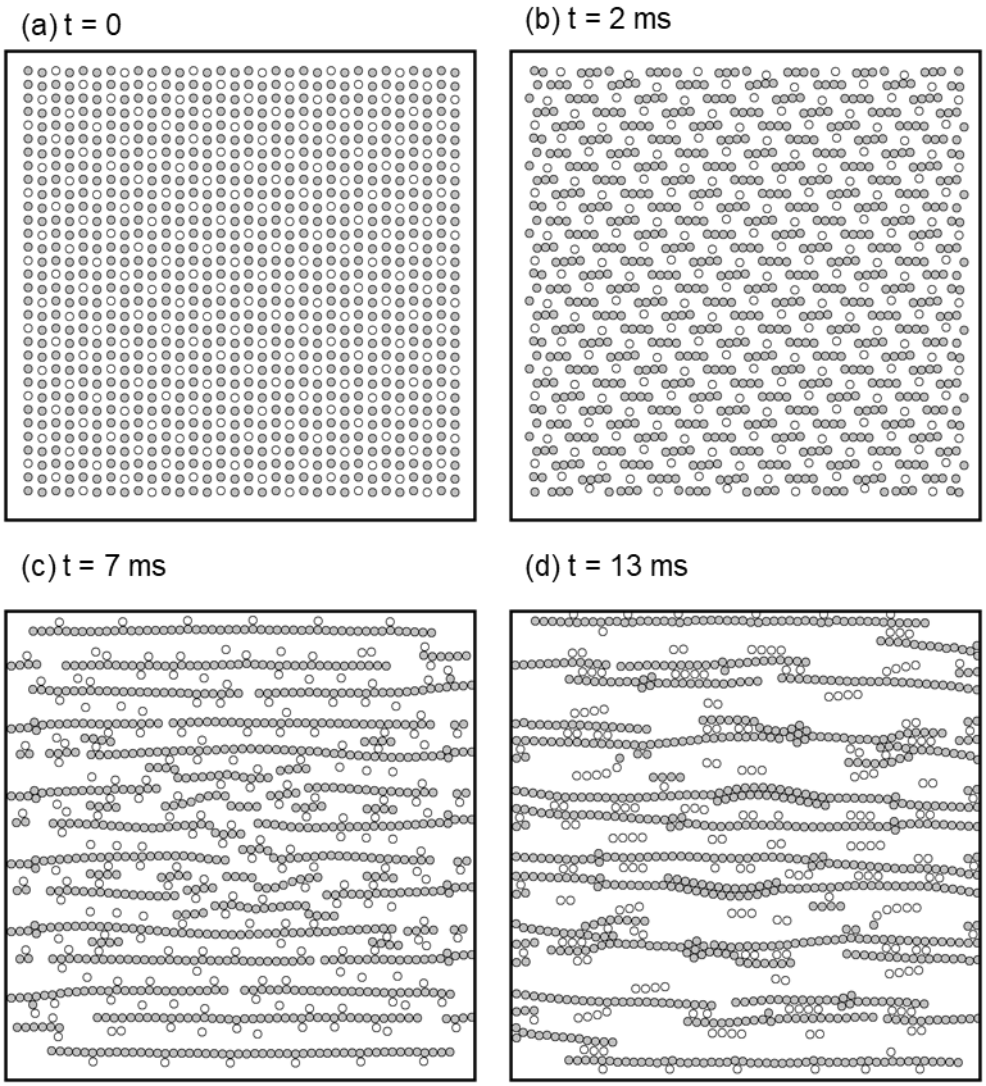

Figure 3.20. Al_2O_3 and $BaTiO_3$ particle positions, at different times in N1 simulation. Al_2O_3 and $BaTiO_3$ indicated by white and gray markers, respectively.

The lower concentration of $BaTiO_3$ particles in N2 results in them acting as a trap for the Al_2O_3 particles, which do not break away from the spade arrangement which is an extension of diamond close pack arrangement to form parallel particle chains like in N1. The stray Al_2O_3 pairs

combine with the extended clusters which continues to grow forming a cellular network of particles with large number of particles as observed in Figure 3.21 (c). The particle clusters shown in Figure 3.21 (d) at t = 36 ms suggests that they become denser by shrinking the gap between the cells of the particle networks. The short Al_2O_3 chains present near the boundary walls move towards the center of the domain to join the extended cluster.

The comparison of Figure 3.20 (d) and 3.21 (d) suggests that presence of Al_2O_3 particles to be less imposing in N1 compared to same number of $BaTiO_3$ particles in N2 which acted as particle traps. The long $BaTiO_3$ chains in N1 form thicker particle clusters by continuing to grow in the vertical direction forming curved particle chains while transporting the Al_2O_3 particles present between the chains towards the end of the chain to attain partial hexagonal close pack arrangement as shown in Figure 3.20 (d). The ejection of Al_2O_3 particles away from the center of the $BaTiO_3$ chains also enables the formation of short Al_2O_3 chains.

The symmetry in particle distributions is maintained because the of the lower composition of opposing p-DEP or n-DEP particles in N1 and N2, respectively. The cluster formation in N1 and N2 simulations due to their dominance of $BaTiO_3$ and Al_2O_3 particles take 13 ms and 36 ms, respectively, which is similar to the time taken by the individual particles in S3 and S5.

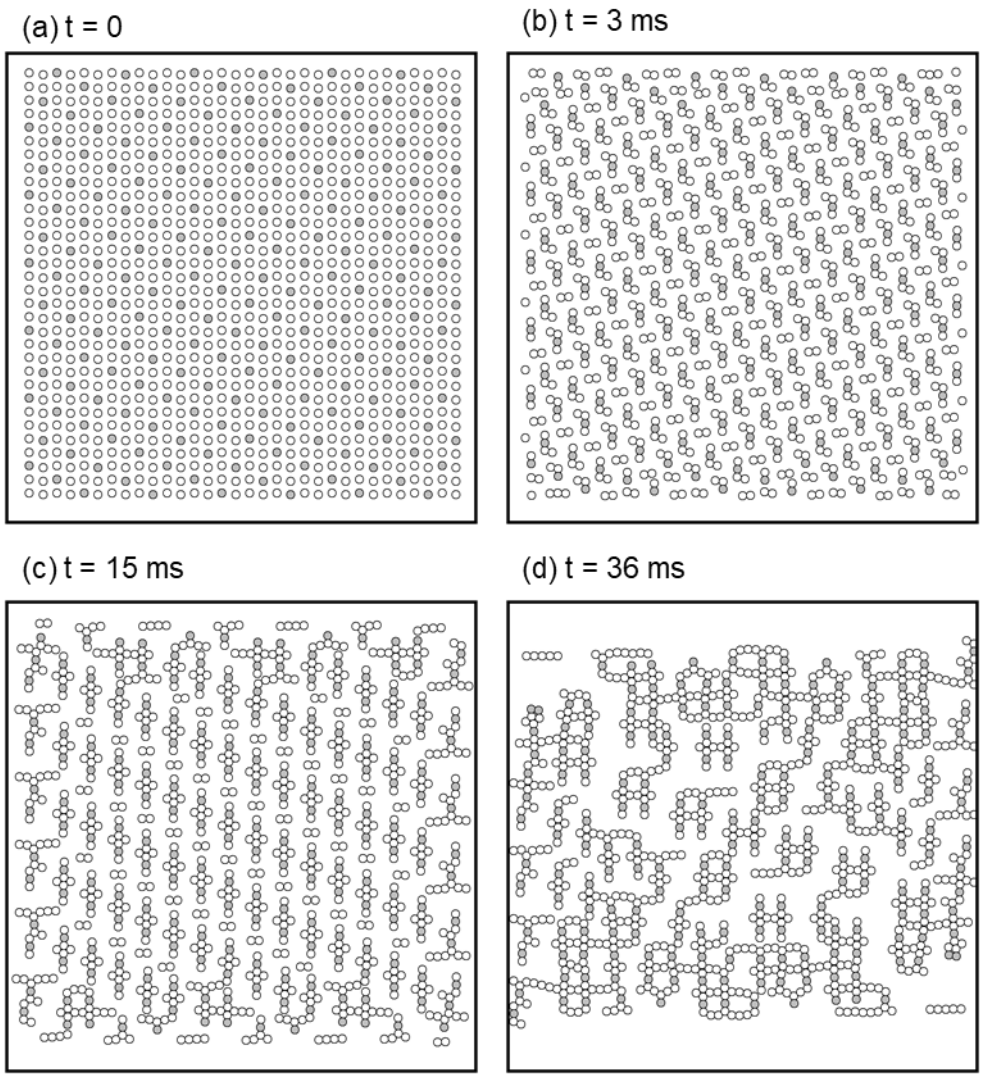

Figure 3.21. Al_2O_3 and $BaTiO_3$ particle positions at different times in N2 simulation. Al_2O_3 and $BaTiO_3$ indicated by white and gray markers, respectively.

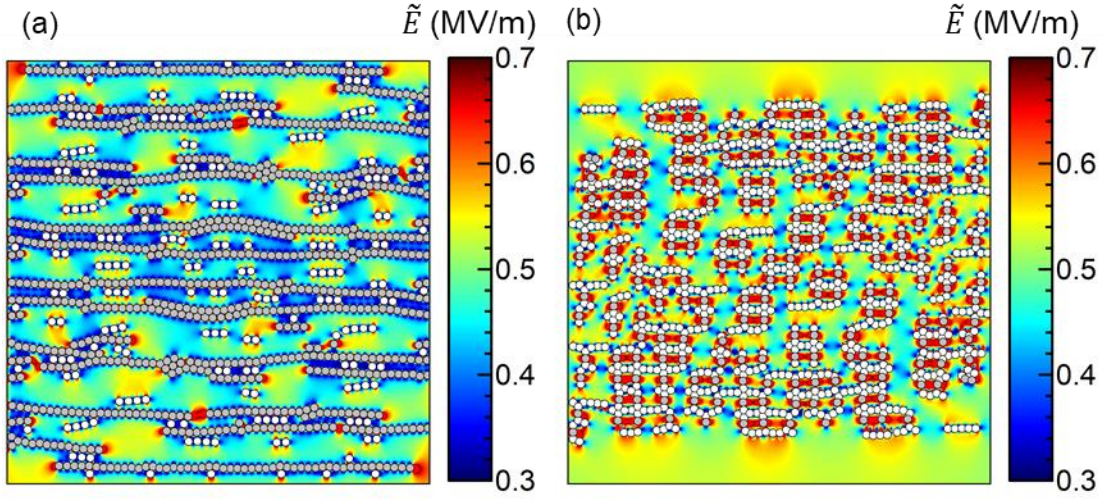

Figure 3.22. Electric field distribution in the 2D domain at the end of (a) N1 and (b) N2 simulations. The gray and white markers represent $BaTiO_3$ and Al_2O_3 particles, respectively.

Figure 3.22 (a) and (b) show the electric field distribution in the 2D domain at the end of simulations N1 and N2, respectively. The high field gradient is observed in domain Figure 3.22 (a) due to the high concentration of $BaTiO_3$ similar to M1, M2, S4 and S5. Low field strength is observed between $BaTiO_3$ particle chains, where the Al_2O_3 particles are mobile. The high electric field regions observed near the ends of $BaTiO_3$ chains indicate curved particle clusters formation that extends between the electrodes. The high field observed near the boundary walls in Figure 3.22 (b) indicate that the Al_2O_3 extended cluster will continue to grow denser towards the center of the domain due to the n-DEP behavior. Although $BaTiO_3$ particles in the spade arrangement are separated by a high field region, they do not form pairs or chains because the Al_2O_3 particles dominate the suspension due to their higher concentration.

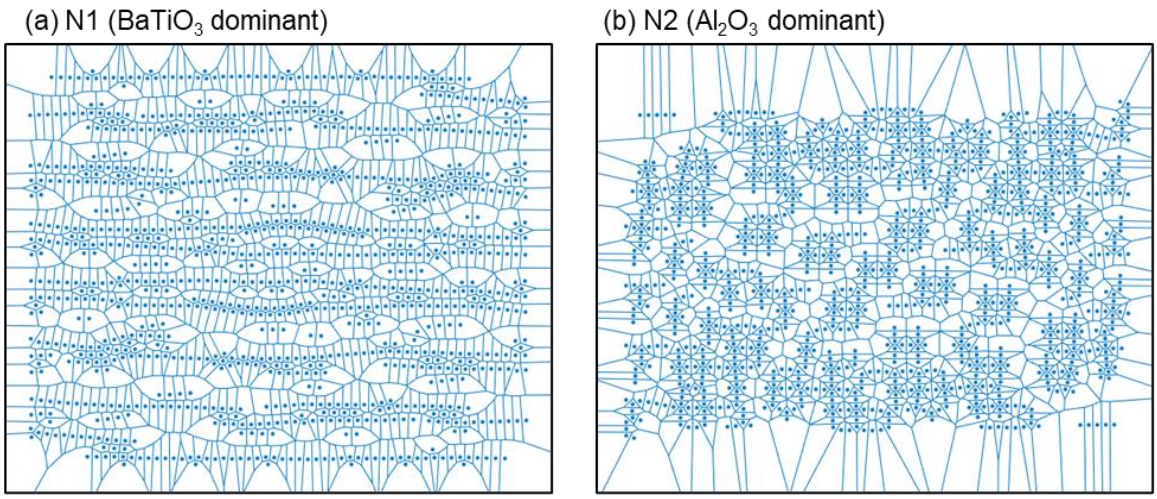

Figure 3.23. Voronoi diagram to estimate the number of geometrical neighbors for the particle distribution at the end of simulation (a) N1 ($BaTiO_3$ dominant suspension) and (b) N2 (Al_2O_3 dominant suspension).

The Voronoi diagram as shown in Figure 3.23 (a) and (b) is used to estimate the number of geometrical neighbors of particles in N1 and N2, respectively. The difference in the average number of geometrical neighbors in N1 and N2, with values 5.970 and 5.951, and the distribution of the geometrical neighbors show in Figure 3.24 (a) suggests scattered isolated particle chains in N1, as opposed to the interconnected clusters in N2. The domain in N2 and N1 have particle arrangement have similar CN_{avg} value of 2.4 and 2.38, respectively. The particle packing in N2 has empty regions in the cluster leading to a slightly higher value than N1 with long separated particle chains. The distribution of structural neighbors for N1 and N2 shown in Figure 3.24 (b), respectively further show the similarity in the dense packing of particles. The major difference in the particle arrangement is conveyed in Figure 3.24 (d) for N1 and N2 showing the distribution of angle made by the structural neighbors with the direction of the field. The significant number of

particles in the spade like arrangement and perpendicular Al_2O_3 - $BaTiO_3$ chains as opposed to the mostly parallel chains in N1 as shown Figure 3.23 (d).

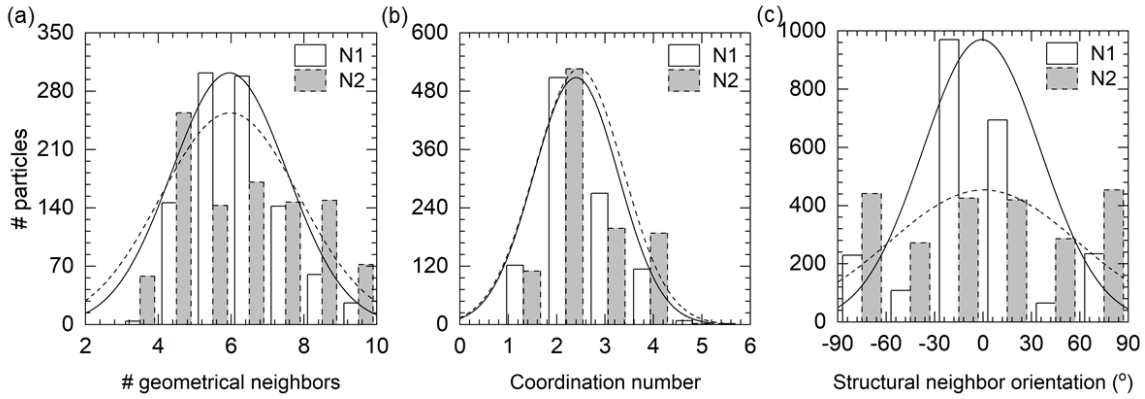

Figure 3.24. Particle packing analysis at the end of simulations N1 and N2. The distribution of (a) number of geometrical neighbors (b) structural neighbors or coordination number and (c) structural neighbor orientation with the direction of the field.

IV. CONCLUSION AND FUTURE WORK

The dielectrophoretic interactive particle motion in 20 vol. % aqueous ceramic suspension with 1024 ceramic particles under AC electric field is investigated using Al_2O_3 and $BaTiO_3$ materials. Multiphysics computational model consisting of validated IDM method, modified Stokes formula, spring force expression are employed to estimate DEP force, hydrodynamic drag force and short- range repulsive forces between non-deformable particles and walls/ electrodes, respectively. The variation of size of the clusters is analyzed for simulations with single type of particles to shed light on the interactive motion and cluster growth with simulation time. The electric field distribution in the domain due to the particle pattern and the corresponding particle packing metrics using Voronoi diagram are evaluated for the final particle arrangement at the end of the simulation.

The simulations S1 - S5 reveal that the pace of particle interaction increases with increase in the magnitude of real (CMF) and favors the particles exhibiting p-DEP behavior. The large difference in simulation time between S1 and S2 - S5 is rationalized by the difference in magnitude of real (CMF) and high amplitude vibrations of the particles at 1 MHz. The effect of high frequency is also observed from the type and number of stable particle arrangements of the particle clusters. The evolution of particle chains into clusters is attributed to the high concentration of the ceramic suspension. The 2D domain at the end of the simulations S1 - S5 and M1 - N1 consists of clusters that are arranged in alternating dense and sparse regions. The regions are particularly distinct in materials with single type of material. The formation of the particle clusters is observed to maintain a symmetry along the center of the domain due to the homogeneous particle size, the shape and size of the domain and the direction of the AC field.

The cluster formation in S1 is slow due to the low frequency but from the electric field distribution they will extend vertically to form clusters of particles in hexagonal close pack arrangement. But absence of clusters with hexagonal close pack arrangement in S2 and S3 with n-DEP Al_2O_3 despite operating at high frequency and high magnitude of real (CMF) is rationalized based on their presence in S4 and S5 with $BaTiO_3$. Therefore, it can be understood that the particle clusters with dense packing are prominent in particles exhibiting p-DEP behavior. This is further reinforced by the observation of small- separated clusters of Al_2O_3 in partial hexagonal arrangement in simulations with mixed type of particles in equal proportion i.e., M1 and M2.

$BaTiO_3$ particles due to their high real (CMF) value and p-DEP nature form large clusters with interconnecting curved segments in S4 and S5. However, the growth of the $BaTiO_3$ clusters is interrupted when Al_2O_3 particles are introduced as they get trapped between $BaTiO_3$ which can be observed M1, M2 and N1. The cluster size and thickness are reduced with increasing proportion of Al_2O_3 particles. However, particle cluster size is maximum in Al_2O_3 rich suspension used in simulation N2. The presence of fewer $BaTiO_3$ acting as particle trap have greater impact than the Al_2O_3 present in the same proportion as seen in N2 and N1, respectively. For suspensions with mixed type of particles, the time taken for cluster formation is equal to the proportion of time consumed by each individual type of particles.

The difference in the initial particle distribution observed in S2 – S5 reveals that, although the closer proximity of particles prompts the formation of particle clusters to occur early, the final particle pattern is largely unaffected in simulations with single material. The difference in particle arrangement pattern at the end of M1 and M2 indicate that the local non-uniformity due to the change in interparticle distance deteriorates the symmetry in the domain as the particles interact and affects the final particle distribution.

The simulation of Al_2O_3 suspensions show a close resemblance in particle arrangement as seen in the average number of geometrical neighbors values of 5.97 and 5.96 and CN_{avg} values of 2.30 and 2.38 at 1 kHZ and 1 MHz, respectively. The average number of structural neighbors reveals that the $BaTiO_3$ ceramic suspension has the most densely packed particle clusters with a value of 2.83, whereas particles in M1 with suspension of Al_2O_3 and $BaTiO_3$ are the most sparsely packed with least CN_{avg} value of 2.25. However, the least average number of geometrical neighbors of value 5.951 and CN_{avg} value of 2.38 for N2 implies that the most interconnected clusters with loose packing can be obtained with large proportion of Al_2O_3 and few $BaTiO_3$. The particle clusters in S1 and N1 are discovered to be the most separated with highest average number of geometrical neighbors of 5.97. The particle packing analysis of M1 and M2 reveal that the smaller interparticle distance results in a tightly packed clusters that are sparsely arranged in the domain.

The data presented in this study shows strong trends in terms of effects of varying frequency, material type, composition of the ceramic materials and initial particle arrangement on the microstructure, final particle packing, and time taken for the particles to form aggregates in the two- dimensional domain. The observed variations are in agreement with the experimental observations [96p] and provide a framework to produce graded ceramic structures using external AC electric field on aqueous ceramic suspensions.

However, in spite of the observed differences in the particle interactions, the variables such as particle size and magnitude of applied AC field that significantly affect the DEP force are worthy of future investigation. The two- dimensional computational domain can also be extended to three- dimensions to facilitate gravitational force to be included in the Multiphysics model,

enabling more robust simulations for external electric field manipulated ceramic fabrication process.

REFERENCES

1. Riedel, R., Ionescu, E., & Chen, I. W. (2008). *Modern trends in advanced ceramics. Ceramics science and technology*, 1, 3-38.
2. Heimann, R. B. (2010). *Classic and advanced ceramics: from fundamentals to applications.* John Wiley & Sons.
3. Evans, A. G. (1982). *Structural reliability: a processing-dependent phenomenon. Journal of the American Ceramic Society*, 65(3), 127-137.
4. Rahaman, M. N. (2017). *Ceramic processing and sintering*. CRC press.
5. Bergstrom, L. (2001). *Colloidal processing of ceramics.* Handbook of Applied Surface and Colloid Chemistry, 1, 201-217.
6. Moreno, R. (2012). *Colloidal processing of ceramics and composites.* Advances in applied ceramics, 111(5-6), 246-253.
7. Adamczyk, Z., & Weroński, P. (1999). *Application of the DLVO theory for particle deposition problems*. Advances in colloid and interface science, 83(1-3), 137-226.
8. Sigmund, W. M., Bell, N. S., & Bergström, L. (2000). *Novel powder-processing methods for advanced ceramics*. Journal of the American Ceramic Society, 83(7), 1557-1574.
9. Lewis, J. A. (2000). *Colloidal processing of ceramics*. Journal of the American Ceramic Society, 83(10), 2341-2359.
10. Zareei, M., Yoozbashizadeh, H., & Hosseini, H. R. M. (2019). *Investigating the effects of pH, surfactant and ionic strength on the stability of alumina/water nanofluids using DLVO theory.* Journal of Thermal Analysis and Calorimetry, 135(2), 1185-1196.

11. Leong, Y. K., Scales, P. J., Healy, T. W., & Boger, D. V. (1995). *Effect of particle size on colloidal zirconia rheology at the isoelectric point.* Journal of the American Ceramic Society, 78(8), 2209-2212.

12. Thompson, J. G., & Mallett, M. W. (1939). *Preparation of Crucibles from Special Refractories by Slip Casting.* Journal of research of the National Bureau of Standards, 23, 319.

13. Howatt, G. N., Breckenridge, R. G., & Brownlow, J. M. (1947). *Fabrication of thin ceramic sheets for capacitors*. Journal of the American Ceramic Society, 30(8), 237-242.

14. Zheng, M., & Zeng, S. Q. (2007). *Analysis of the sintered temperature and mechanical properties of the sic ceramics made by injection molding*. Journal of Shaanxi University of Science & Technology (Natural Science Edition), 6.

15. Graule, T. J., Baader, F. H., & Gauckler, L. J. (1995). *Casting uniform ceramics with direct coagulation*. Chemtech-Washington DC-, 25, 31-31.

16. Banda, M., Akurati, S., & Ghosh, D. (2020). *Governing role of the ratio of large platelet particles to ultrafine particles on dynamic and quasistatic compressive response and damage evolution in ice-templated alumina ceramics*. Journal of Materials Research, 35(21), 2870-2886.

17. Halloran, J. W. (2016). *Ceramic stereolithography: additive manufacturing for ceramics by photopolymerization.* Annual Review of Materials Research, 46, 19-40.

18. Agarwala, M. K., Weeren, R. V., Vaidyanathan, R., Bandyopadhyay, A., Carrasquillo, G., Jamalabad, V., & Ballard, C. (1995). *Structural ceramics by fused deposition of ceramics*. International Solid Freeform Fabrication Symposium.

19. Cesarano III, J., King, B. H., & Denham, H. B. (1998). *Recent developments in robocasting of ceramics and multimaterial deposition* (No. SAND-98-2195C; CONF-980826-). Sandia National Labs., Albuquerque, NM.

20. Cima, M. J., Oilveira, M., Wang, H. R., Sachs, E., & Holman, R. (2001). *Slurry-based 3DP and fine ceramic components*. International Solid Freeform Fabrication Symposium.

21. Fukasawa, T., Ando, M., & Ohji, T. (2002). *Filtering properties of porous ceramics with unidirectionally aligned pores.* Journal of the Ceramic Society of Japan, 110(1283), 627-631.

22. Fukushima, M., & Yoshizawa, Y. I. (2014). *Fabrication of highly porous silica thermal insulators prepared by gelation–freezing route*. Journal of the American Ceramic Society, 97(3), 713-717.

23. Bobkova, N. M., Zayats, N. I., Kolontaeva, T. V., Pun'ko, G. N., & Zakharevich, G. B. (2000). *Porous glass ceramic bioimplants*. Glass and ceramics, 57(11), 412-414.

24. Lo, Y. W., Wei, W. C. J., & Hsueh, C. H. (2011). *Low thermal conductivity of porous Al_2O_3 foams for SOFC insulation*. Materials Chemistry and Physics, 129(1-2), 326-330.

25. Sakka, Y., Tang, F., Fudouzi, H., & Uchikoshi, T. (2005). *Fabrication of porous ceramics with controlled pore size by colloidal processing*. Science and Technology of Advanced Materials, 6(8), 915.

26. Galassi, C. (2006). *Processing of porous ceramics: Piezoelectric materials*. Journal of the European Ceramic Society, 26(14), 2951-2958.

27. Baba, S., Harada, T., Shimizu, H., Doshida, Y., & Tanaka, S. (2016). *Colloidal processing using UV curable resin under high magnetic field for textured ceramics*. Journal of the European Ceramic Society, 36(11), 2739-2743.

28. Makiya, A., Kusumi, Y., Tanaka, S., Kato, Z., Uchida, N., Uematsu, K., & Kitazawa, K. (2007). *Grain oriented titania ceramics made in high magnetic field*. Journal of the European Ceramic Society, 27(2-3), 797-799.

29. Li, M., Li, W. H., Zhang, J., Alici, G., & Wen, W. (2014). *A review of microfabrication techniques and dielectrophoretic microdevices for particle manipulation and separation.* Journal of Physics D: Applied Physics, 47(6), 063001.

30. Al-Faqheri, W., Thio, T. H. G., Qasaimeh, M. A., Dietzel, A., & Madou, M. (2017). *Particle/cell separation on microfluidic platforms based on centrifugation effect: a review*. Microfluidics and Nanofluidics, 21(6), 1-23.

31. Takagi, J., Yamada, M., Yasuda, M., & Seki, M. (2005). *Continuous particle separation in a microchannel having asymmetrically arranged multiple branches.* Lab on a Chip, 5(7), 778-784.

32. Yamada, M., & Seki, M. (2005). *Hydrodynamic filtration for on-chip particle concentration and classification utilizing microfluidics.* Lab on a Chip, 5(11), 1233-1239.

33. Nasiri, R., Shamloo, A., Ahadian, S., Amirifar, L., Akbari, J., Goudie, M. J., ... & Khademhosseini, A. (2020*). Microfluidic-based approaches in targeted cell/particle separation based on physical properties: Fundamentals and Applications.* Small, 16(29), 2000171.

34. Franks, G. V., Tallon, C., Studart, A. R., Sesso, M. L., & Leo, S. (2017). *Colloidal processing: enabling complex shaped ceramics with unique multiscale structures.* Journal of the American Ceramic Society, 100(2), 458-490.

35. Niu, F., Wu, D., Ma, G., Wang, J., Guo, M., & Zhang, B. (2015). *Nanosized microstructure of Al_2O_3–ZrO_2 (Y_2O_3) eutectics fabricated by laser engineered net shaping.* Scripta Materialia, 95, 39-41.

36. Oberti, S., Moeller, D., Neild, A., Dual, J., Beyeler, F., Nelson, B. J., & Gutmann, S. (2010). *Strategies for single particle manipulation using acoustic and flow fields.* Ultrasonics, 50(2), 247-257.

37. Miyagawa, A., & Okada, T. (2020). *Particle Manipulation with External Field; From Recent Advancement to Perspectives*. Analytical Sciences, 20SAR03.

38. Ogden, T. A., Prisbrey, M., Nelson, I., Raeymaekers, B., & Naleway, S. E. (2019). *Ultrasound freeze casting: Fabricating bioinspired porous scaffolds through combining freeze casting and ultrasound directed self-assembly*. Materials & Design, 164, 107561.

39. Van Reenen, A., de Jong, A. M., den Toonder, J. M., & Prins, M. W. (2014). *Integrated lab-on-chip biosensing systems based on magnetic particle actuation– a comprehensive review*. Lab on a Chip, 14(12), 1966-1986.

40. Sato, K., Mishra, M., Hirano, H., Suzuki, T. S., & Sakka, Y. (2014). *Fabrication of textured Ti_3SiC_2 ceramic by slip casting in a strong magnetic field and pressureless sintering.* Journal of the Ceramic Society of Japan, 122(1429), 817-821.

41. Zhang, S., Wang, Y., Onck, P., & den Toonder, J. (2020). *A concise review of microfluidic particle manipulation methods.* Microfluidics and Nanofluidics, 24(4), 1-20.

42. Ghrairi, N., & Bouaicha, M. (2012). *Structural, morphological, and optical properties of TiO_2 thin films synthesized by the electrophoretic deposition technique*. Nanoscale research letters, 7(1), 1-7.

43. Hu, S., Li, W., Li, W., Zhang, N., Qi, H., Finklea, H., & Liu, X. (2019). A study on the electrophoretic deposition of gadolinium doped ceria on polypyrrole coated yttrium stabilized zirconia. Journal of colloid and interface science, 555, 115-123.

44. Heavens, S. N. (1990). *Electrophoretic deposition as a processing route for ceramics*. Noyes Publications, Advanced Ceramic Processing and Technology., 1, 255-283.

45. D'Ambrogio, G. (2019). *Piezoelectric composites structured via dielectrophoresis for sensor applications*.

46. Sonnenberg, A., Marciniak, J. Y., McCanna, J., Krishnan, R., Rassenti, L., Kipps, T. J., & Heller, M. J. (2013). *Dielectrophoretic isolation and detection of cfc-DNA nanoparticulate biomarkers and virus from blood*. Electrophoresis, 34(7), 1076-1084.

47. Lorenz, M., Malangré, D., Du, F., Baune, M., Thöming, J., & Pesch, G. R. (2020). *High-throughput dielectrophoretic filtration of sub-micron and micro particles in macroscopic porous materials.* Analytical and bioanalytical chemistry, 412(16), 3903.

48. Hoffman, P. D., Sarangapani, P. S., & Zhu, Y. (2008). *Dielectrophoresis and AC-induced assembly in binary colloidal suspensions.* Langmuir, 24(21), 12164-12171.

49. Ahadian, S., Naito, U., Surya, V. J., Darvishi, S., Estili, M., Liang, X., & Matsue, T. (2017). *Fabrication of poly (ethylene glycol) hydrogels containing vertically and horizontally aligned graphene using dielectrophoresis: an experimental and modeling study*. Carbon, 123, 460-470.

50. Hung, C. L., Kao, Y. C., & Juang, J. Y. (2021). *Dielectrophoretic crossover frequency of individual pearl chains formed by bonded colloidal spheres*. Sensors and Actuators B: Chemical, 327, 128888.

51. Javidi, R., Zand, M. M., & Dastani, K. (2019). *Dielectrophoretic interaction of two particles in a uniform electric field.* Microsystem Technologies, 25(7), 2699-2711.

52. Van den Ende, D. A., Bory, B. F., Groen, W. A., & Van Der Zwaag, S. (2010). *Properties of quasi 1-3 piezoelectric PZT-epoxy composites obtained by dielectrophoresis*. Integrated Ferroelectrics, 114(1), 108-118.

53. Kim, G., & Shkel, Y. M. (2004). *Polymeric composites tailored by electric field.* Journal of materials research, 19(4), 1164-1174.

54. Xuan, X. (2019). *Recent advances in direct current electrokinetic manipulation of particles for microfluidic applications*. Electrophoresis, 40(18-19), 2484-2513.

55. Velev, O. D., & Bhatt, K. H. (2006). *On-chip micromanipulation and assembly of colloidal particles by electric fields.* Soft Matter, 2(9), 738-750.

56. Sridharan, S., Zhu, J., Hu, G., & Xuan, X. (2011). *Joule heating effects on electroosmotic flow in insulator-based dielectrophoresis*. Electrophoresis, 32(17), 2274-2281.

57. Kadaksham, J., Singh, P., & Aubry, N. (2006). *Manipulation of particles using dielectrophoresis.* Mechanics Research Communications, 33(1), 108-122.

58. Hossan, M. R., Gopmandal, P. P., Dillon, R., & Dutta, P. (2016). *A comprehensive numerical investigation of DC dielectrophoretic particle- particle interactions and assembly.* Colloids and Surfaces A: Physicochemical and Engineering Aspects, 506, 127-137.

59. Jones, T. B. (2003). *Basic theory of dielectrophoresis and electrorotation*. IEEE Engineering in medicine and Biology Magazine, 22(6), 33-42.

60. Wang, X., Wang, X. B., & Gascoyne, P. R. (1997). *General expressions for dielectrophoretic force and electrorotational torque derived using the Maxwell stress tensor method.* Journal of electrostatics, 39(4), 277-295.

61. Zhang, Q., & Zhang, K. (2018). *Iterative dipole moment method for the dielectrophoretic particle-particle interaction in a dc electric field*. Journal of nanotechnology.

62. Aubry, N., & Singh, P. (2006). *Control of electrostatic particle-particle interactions in dielectrophoresis.* EPL (Europhysics Letters), 74(4), 623.

63. Ai, Y., Zeng, Z., & Qian, S. (2014). *Direct numerical simulation of AC dielectrophoretic particle–particle interactive motions*. Journal of colloid and interface science, 417, 72-79.

64. Liu, L., Xie, C., Chen, B., & Wu, J. (2015). *Iterative dipole moment method for calculating dielectrophoretic forces of particle-particle electric field interactions.* Applied Mathematics and Mechanics, 36(11), 1499-1512.

65. Derakhshan, R., Ramiar, A., & Ghasemi, A. (2020). *Numerical investigation into continuous separation of particles and cells in a two-component fluid flow using dielectrophoresis*. Journal of Molecular Liquids, 310, 113211.

66. Li, J., Zhang, Q., Peng, N., & Zhu, Q. (2005). *Manipulation of carbon nanotubes using AC dielectrophoresis*. Applied Physics Letters, 86(15), 153116.

67. Çetin, B., & Li, D. (2011). *Dielectrophoresis in microfluidics technology.* Electrophoresis, 32(18), 2410-2427.

68. Qian, C., Huang, H., Chen, L., Li, X., Ge, Z., Chen, T., & Sun, L. (2014). *Dielectrophoresis for bioparticle manipulation*. International Journal of Molecular Sciences, 15(10), 18281-18309.

69. Liu, L., Xie, C., Chen, B., Chiu-On, N., & Wu, J. (2016). *A new method for the interaction between multiple DEP particles: iterative dipole moment method.* Microsystem Technologies, 22(9), 2223-2232.

70. Xie, C., Chen, B., Liu, L., Chen, H., & Wu, J. (2016). *Iterative dipole moment method for the interaction of multiple dielectrophoretic particles in an AC electrical field.* European Journal of Mechanics-B/Fluids, 58, 50-58.

71. Hossan, M. R., Dillon, R., Roy, A. K., & Dutta, P. (2013). *Modeling and simulation of dielectrophoretic particle–particle interactions and assembly.* Journal of colloid and interface science, 394, 619-629.

72. Hu, S., & Fu, R. (2019). *Expanding the flexibility of dynamics simulation on different size particle–particle interactions by dielectrophoresis*. Journal of biological physics, 45(1), 45-62.

73. Barsoum, M. W. (2019). *Fundamentals of ceramics.* CRC press.

74. Auerkari, P. (1996). *Mechanical and physical properties of engineering alumina ceramics* (Vol. 23). Espoo: Technical Research Centre of Finland.

75. Nowotny, J., & Rekas, M. (1991). *Positive temperature coefficient of resistivity for $BaTiO_3$-based materials*. Ceramics international, 17(4), 227-241.

76. Wu, L., Chure, M. C., Wu, K. K., Chang, W. C., Yang, M. J., Liu, W. K., & Wu, M. J. (2009). *Dielectric properties of barium titanate ceramics with different materials powder size*. Ceramics International, 35(3), 957-960.

77. Zhao, S. C., Sidle, S., Swinney, H. L., & Schröter, M. (2012). *Correlation between Voronoi volumes in disc packings*. EPL (Europhysics Letters), 97(3), 34004.

78. Haughey, D. P., & Beveridge, G. S. G. (1969). *Structural properties of packed beds—a review*. The Canadian Journal of Chemical Engineering, 47(2), 130-140.

79. Gervois, A., Oger, L., Richard, P., & Troadec, J. P. (2002, April). *Voronoi and radical tessellations of packings of spheres.* International Conference on Computational Science (pp. 95-104). Springer, Berlin, Heidelberg.

80. Chen, V., & Hlavacek, M. (1994). *Application of Voronoi tessellation for modeling randomly packed hollow-fiber bundles.* AIChE journal, 40(4), 606-612.

81. Tanemura, M. (1988). *Random packing and random tessellation in relation to the dimension of space.* Journal of microscopy, 151(3), 247-255.

82. Gervois, A., Troadec, J. P., & Lemaitre, J. (1992). *Universal properties of Voronoi tessellations of hard discs*. Journal of Physics A: Mathematical and General, 25(23), 6169.

83. Bormashenko, E., Frenkel, M., Vilk, A., Legchenkova, I., Fedorets, A. A., Aktaev, N. E., & Nosonovsky, M. (2018). *Characterization of self-assembled 2D patterns with Voronoi Entropy*. Entropy, 20(12), 956.

84. Tsaur, J. Y. (1988). *An analysis of the dense packing of disks: a computer simulated approach.*

85. Archer, D. G., & Wang, P. (1990). *The dielectric constant of water and Debye-Hückel limiting law slopes*. Journal of physical and chemical reference data, 19(2), 371-411.

86. Xie, C., Chen, B., Liu, L., Chen, H., & Wu, J. (2016). *Iterative dipole moment method for the interaction of multiple dielectrophoretic particles in an AC electrical field.* European Journal of Mechanics-B/Fluids, 58, 50-58.

87. Liu, L., Xie, C., Chen, B., & Wu, J. (2016*). Numerical study of particle chains of a large number of randomly distributed DEP particles using iterative dipole moment method.* Journal of Chemical Technology & Biotechnology, 91(4), 1149-1156.

88. Gascoyne, P. R., & Vykoukal, J. (2002). *Particle separation by dielectrophoresis.* Electrophoresis, 23(13), 1973–1983.

89. Chen, Q., & Yuan, Y. J. (2019). *A review of polystyrene bead manipulation by dielectrophoresis.* RSC advances, 9(9), 4963-4981.

90. Xie, C., Chen, B., Ng, C. O., Zhou, X., & Wu, J. (2015). *Numerical study of interactive motion of dielectrophoretic particles.* European Journal of Mechanics-B/Fluids, 49, 208-216.

VITA

Naga Bharath Gundrati was born in Hyderabad, TG, INDIA on December 21st, 1993. He graduated from SRM University in Chennai in 2015 with a Bachelor of Technology degree in Mechanical Engineering. Following his undergraduate education, he attended State University of New York at Buffalo to obtain his Master of Science degree in Mechanical and Aerospace Engineering. There he worked on self- sensing capabilities of polymeric resin used in 3D printing stereolithography technique under the guidance of Dr. Deborah Chung. After gaining knowledge on polymer materials, he then returned to his home in India to work at a pharmaceutical company, Rashmi Pharma Pvt. Ltd., to support his family. To further advance his academic and technical knowledge in the field of mechanical engineering, he joined the Master of Science program in Mechanical and Aerospace Engineering at Old Dominion University in Norfolk, VA. At ODU, he has worked under the guidance of Dr. Dipankar Ghosh in the Laboratory of Advanced Manufacturing of Materials from fall 2019 to summer 2021 where he learned about ceramics and their processing in detail.